Scientia Pharmaceutica

ÖSTERREICHISCHE PHARMAZEUTISCHE GESELLSCHAFT

MDPI

Article

Repurposing of Four Drugs as Anti-SARS-CoV-2 Agents and Their Interactions with Protein Targets

Luis C. Vesga [1], Camilo A. Ruiz-Hernández [1], Jeimmy J. Alvarez-Jacome [1], Jonny E. Duque [2], Bladimiro Rincon-Orozco [1,3] and Stelia C. Mendez-Sanchez [1,3,*]

[1] Grupo de Investigación en Bioquímica y Microbiología (GIBIM), Universidad Industrial de Santander A. A. 678, Piedecuesta 681027, Colombia; luis.vesga@correo.uis.edu.co (L.C.V.); camilo2162151@correo.uis.edu.co (C.A.R.-H.); jeimmy2171468@correo.uis.edu.co (J.J.A.-J.); blrincon@uis.edu.co (B.R.-O.)

[2] Centro de Investigación en Enfermedades Tropicales (CINTROP), Universidad Industrial de Santander A. A. 678, Piedecuesta 681027, Colombia; jonedulu@uis.edu.co

[3] Grupo de Investigación en Compuestos Orgánicos de Interés Medicinal CODEIM, Universidad Industrial de Santander A. A. 678, Piedecuesta 681027, Colombia

* Correspondence: scmendez@uis.edu.co

Abstract: Although there are existing vaccines against severe acute respiratory syndrome coronavirus-2 (SARS-CoV-2), new COVID-19 cases are increasing due to low immunization coverage and the emergence of new variants. For this reason, new drugs to treat and prevent severe COVID-19 are needed. Here, we provide four different FDA-approved drugs against SARS-CoV-2 proteins involved in the entry and replication process, aiming to identify potential drugs to treat COVID-19. We use the main protease (M^{pro}), the spike glycoprotein (S protein), and RNA-dependent RNA polymerase (RdRp) as protein targets for anti- SARS-CoV-2 drugs. In our constructed database, we selected different drugs against each target (M^{pro}, S protein, and RdRp) based on their common interactions with relevant residues involved in viral entry at the host cell and replication. Furthermore, their stability inside the binding pocket, as well as their predicted binding-free energy, allow us to provide new insight into the possible drug repurposing of viomycin (interacting with M^{pro}) due to its interactions with key residues, such as Asn 143, Glu 166, and Gln 189 at the same time as hesperidin (interacting with the S protein) is interacting with residues Tyr 449, Ser 494, and Thr 500, keeping inside the predicted binding pocket, as well as interacting with residues in different variants of concern. Finally, we also suggest nystatin and elvitegravir (interacting with RdRp) as possible drugs due to their stability within the predicted pocket along the simulation and their interaction with key residues, such as Asp 760, Asp 761, and Asp 618. Altogether our results provide new knowledge about the possible mechanism of the inhibition of viomycin, hesperidin, elvitegravir, and nystatin to inhibit the viral life cycle of SARS-CoV-2 and some of its variants of concern (VOC). Additionally, some iodide-based contrast agents were also found to bind the S protein strongly, i.e., iohexol (−58.99 Kcal/mol), iotrolan (−76.19 Kcal/mol), and ioxilan (−62.37 Kcal/mol). Despite the information we report here as the possible strong interaction between these contrast agents and the SARS-CoV-2's S protein, M^{pro}, and RdRp, we believe that further investigation, including chemical modifications in their structures, are needed for COVID-19 treatment.

Keywords: repurposing drugs; COVID; SARS-CoV-2; molecular docking

Citation: Vesga, L.C.; Ruiz-Hernández, C.A.; Alvarez-Jacome, J.J.; Duque, J.E.; Rincon-Orozco, B.; Mendez-Sanchez, S.C. Repurposing of Four Drugs as Anti-SARS-CoV-2 Agents and Their Interactions with Protein Targets. *Sci. Pharm.* **2022**, *90*, 24. https://doi.org/10.3390/scipharm90020024

Academic Editor: Helen D. Skaltsa

Received: 14 February 2022
Accepted: 26 March 2022
Published: 14 April 2022

1. Introduction

The coronavirus disease of 2019—COVID-19 is caused by a severe acute respiratory syndrome coronavirus-2 (SARS-CoV-2) [1]. Within coronaviruses, SARS-CoV-2, SARS-CoV-1, and MERS-CoV belong to the genus betacoronavirus, characterized by a highly contagious rate and causing a wide variety of illnesses with neurological, respiratory, enteric, and hepatic manifestations [2–4].

Betacoronaviruses are enveloped positive-sense single-stranded RNA viruses with a symmetrical nucleocapsid [5]. Mainly, SARS-CoV-2's genetic organization comprises 27 proteins encoded by 14 open-reading frames (ORFs), where ORF1 and ORFb encode four polyproteins after proteolytic processes produce 16 non-structural proteins (NSP) directly involved in RNA replication and transcription [5,6]. Furthermore, structural proteins, such as the spike, envelope, membrane, and nucleocapsid, are encoded in the adjacent region to 3′-end and some accessory proteins [1,7].

Within these proteins, the main protease (M^{pro}), viral the spike glycoprotein (S protein), and RNA-dependent RNA polymerase (RdRp), and others are identified as potential drug targets to prevent infection with and act as a treatment for COVID-19 [8,9]. M^{pro} is responsible for viral polyprotein cleavage to functional units, playing a pivotal role in viral replication, transcription, and packaging within the host cell [10,11].

In this sense, the drug design strategy against the SARS-CoV-2 virus can be divided into two different strategies: the pre-fusion stage, where targeting the spike glycoprotein of SARS-CoV-2, including its domains S1 and S2 and its consequence membrane fusion, is one of the leading options in vaccines and antiviral drug compounds [12,13]. On the other hand, in the second strategy, the post-fusion stage involves targeting the viral proteins after replication within the host cell where targeting the SARS-CoV-2 main protease (M^{pro}) is included, but also, RNA-dependent RNA polymerase has arisen as an essential target in drug development against coronaviruses [8,14].

Since M^{pro} is unique to the virus, targeting and successfully inhibiting its protease activity makes M^{pro} an interesting druggable target [15].

M^{pro} is a cysteine protease and structurally comprises 306 amino acids organized into three different domains, distributed as follows [8,16]: domain I (residues 8–101), domain II (residues 102–184), and domain III (residues 201–303). Additionally, a long loop required for dimerization is located between residues 185–200, connecting the domains II and III [17], and its catalytic site is on the interface of domains I and II, forming a cleft with residues His 41 and Cys 145 as a catalytic dyad [17,18]. Moreover, some authors have subdivided this active site into S1′, S1, S2, and S4 (Figure S1), where more of the M^{pro} covalent inhibitors form a covalent bond with the thiol group of Cys 145 located at S1 [18–20]. The subsite S1 is formed by Phe 140, Leu 141, Asn 142, His 163, Glu 166, and His 172. Then, in a small cavity separated by Asn 142 residue is located the subsite S1′, comprised of the residues Thr 25, Thr 26, and Leu 127. A hydrophobic S2 site is formed by the residues His 41, Met 49, Tyr 54, and Met 165. Finally, the subsite S4 is comprised of Met 165, Leu 167, Phe 185, Gln 189, and Gln 194 amino acid residues [8].

Transmembrane the spike (S) glycoprotein provides a cellular mechanistic for coronavirus infections because it is pivotal in the entry of the virus into host cells by using the specific receptor ACE-2 [5,21]. The viral load and replication are correlated with the affinity binding of the S protein ACE2 receptor and TMPRSS2 protease activity in the host cell [10,22–24].

Moreover, the S protein is essential for SARS-CoV-2 entry into the host cells, forming a homotrimer at the viral surface [21]. The S protein has two different domains (herein called S1 and S2), where the S1 domain has a direct role in the direct interaction with the ACE2 receptor at the host cell while the S2 domain is responsible for the viral and receptor membrane fusion [13,24].

Furthermore, RdRp is an essential target since RNA polymerase is a vital enzyme for viral replication/transcription [25]. The coronaviruses' replication is mediated by a replication-and-transcription complex comprised of viral non-structural proteins (nsps), wherein the principal component of this complex is the non-structural protein nsp12 [26,27]. By itself, nsps12 has biological activity, but its function also requires nsps7 and nsp8 to complete the overall arrangement observed in the SARS-CoV structure [14,28,29]. Recently, Yi. et al., 2021, elucidated a crystal structure of SARS-CoV-2 RdRp, where nsp12 also contains an N-terminal domain (residues 30 to 50), with a finger configuration (residues 397 to 581 and 621 to 679), really closely forming a small circle with the thumb subdomain

(residues 819 to 920) [14,30]. In this way, the closed conformation of nsp12 is stabilized by the nsp7–nsp8 dimer. Two zinc ions were found at metal-binding motifs (consisting of His295-Cys301-Cys306-Cys310 and Cys487-His642-Cys645-C646); its function is likely to maintain the structural RdRp architecture [29].

Furthermore, the RdRp crystal structure contains 14-base RNA in the template strand and the inhibitor remdesivir monophosphate (RMP), which is covalently joined to the primer strand and two magnesium ions near the active site that may enhance the catalytic function [14,31]. Remdesivir as an adenosine monophosphate analog inhibits the RdRp, making a solid interaction with the primer strand and two hydrogen bonds with the uridine base. Additionally, RMP interacts with the side chain of residues Lys 545 and Arg 555, finding magnesium ions and pyrophosphate groups near the protein's active site [14]. In addition to RMP, antivirals or nucleotides analog drugs, such as galidesivir, favipiravir, and ribavirin, have been reported as SARS-CoV-2 inhibitors because they inhibit RdRp and viral replication in cell-based assays [32,33].

COVID-19 is highly infectious, and since its onset in December 2019, more than 266 million cases have been reported according to the World Health Organization (WHO). Despite the newly developed vaccines and the continued decrease in the new COVID-19 cases, low immunization coverage and the emergence of new variants are changing this situation [34,35]. In the continued search for new treatments against COVID-19, focus not only on vaccines is needed. This study aims to identify and report potential candidate drugs using a computational approach, such as molecular docking and molecular dynamics simulations using an FDA-approved drug library, to evaluate their potential for repurposing against SARS-CoV-2 and its relevant variants.

2. Materials and Methods

2.1. Drug Database Construction and Ligand Preparation

A total of 14,347 compounds was retrieved from the ChEMBL and DrugBank databases. All compounds were visualized and prepared using Maestro and LigPrep [36] to generate the three-dimensional conformation, calculate the partial atomic charges, and adjust the protonation states at pH 7.4 using the force field OPLS4 [37].

2.2. Protein Preparation and Molecular Docking

The protein preparation and docking calculations were performed using the Schrödinger Drug Discovery Suite for molecular modeling (version 2021–1). The crystal structure of SARS-CoV-2 M^{pro} (PDB ID: 6LU7, resolution 2.16 Å [18]); the spike glycoprotein (PDB ID: 6M0J, resolution 2.45 Å [38]); and RNA-dependent RNA polymerase from SARS-CoV-2 (PDB ID: 7BV2, resolution 2.5 Å [14]) were obtained from the Protein Data Bank (PDB, www.rcsb.org), and prepared using the Protein Preparation Wizard [39] to fix the protonated states of amino acids residues, adding polar hydrogens and missing side-chain atoms using Prime [40].

Molecular docking studies were performed with the prepared ligands using Glide (v8.9) with three precision settings. For this, Glide offers a full range of accurate docking options from the HTVS (high-throughput virtual screening) mode to the SP (standard precision) mode and, finally, the XP (extra precision) mode [41,42]. For M^{pro}, the spike glycoprotein, and RNA-dependent RNA polymerase, ligands were docked in a grid box of 25 Å as follows. For the main protease (M^{pro}), the receptor grid was generated by indicating the coordinates of active site amino acid residues, centered at x = 7.974, y = 3.29, and z = 19.645. The receptor grid for the spike glycoprotein (S protein) was generated according to Unni et al., 2020 [13], where three different sites were previously identified at the interface between the spike glycoprotein and the ACE2 receptor. For this, the grid receptor at site 1 was centered in residues Gln 498, Thr 500, and Asn 501, while the grid receptor at site 2 was centered in residues Lys 417 and Tyr 453. Finally, at site 3, the grid box was settled in residues Gln 474 and Phe 486. RNA-dependent RNA polymerase was also prepared, and all ions, except the magnesium from the active site, and non-relevant

crystallographic materials were removed. The docking box of 12 Å was centered at the same place as the co-crystallized ligand Remdesivir (RMP) according to Ahmad et al., 2020 [43]. Docking poses were selected by visual inspection based on their common interactions with relevant residues for each target.

2.3. Free Energy Binding Calculations (MM-GBSA)

Molecular mechanics, the Generalized Born model, and solvent-accessibility (MM-GBSA) analysis were performed to predict the binding-free energy of selected ligand-protein complexes [44,45]. For this, the Prime module of the Schrödinger Drug Discovery Suite was used to calculate the binding energy of selected ligands in complex with the protein target. For the analysis, Prime MM-GBSA calculates the energy of optimized free receptors, free ligands, and protein–ligand complexes. It also calculates the ligand strain energy by placing ligands in a solution generated by the VSGB 2.0 Suite and OPLS3e force field [46].

2.4. Molecular Dynamics Simulation

In this work, overall, twenty-one MD simulations of 100 ns each were performed, where selected poses from the docking for each target were validated by molecular dynamics simulation, and ligand stability within the proposed pocket and its interactions were evaluated. MD simulations were performed using Desmond [47] with the OPLS4 force field [37,48], which led to improved performance in predicting protein–ligand binding affinities. Protein–ligand systems were placed in a cubic box with 7 Å from the edges to any atoms of the system using the System Builder. Additionally, the cubic box was filled with TIP3P [49] water, and the systems were neutralized by adding Na^+ or Cl^- ions according to the system charge, and PBC conditions were used. For all systems, the NPT ensemble class was chosen, and short simulations equilibrated systems for 5 ns implementing the Berendsen thermostat and Barostat methods were used. From the beginning to the end of the simulations, a constant temperature of 310 K and 1 atm of pressure were kept using the Nose–Hoover thermostat algorithm and the Martyna–Tobias–Klein Barostat algorithm. After minimization and relaxing steps, we proceeded with the production step of 100 ns, and all MD simulations were performed with at least three independent runs with randomly generated seeds.

Protein–ligand interactions, along with the simulations and protein conformational changes, were analyzed using the Simulation Interaction Diagram (SID) available in Maestro. The root mean square deviation (RMSD) and root mean square fluctuation (RMSF) of the protein and ligand were used to check the MD simulation stability along the 100 ns.

2.5. Visualization

Docking images were generated using PyMOL 2.4.1 [50], and graphs were plotted using GraphPad version 8.1 for Windows, GraphPad Software (San Diego, CA, USA, www.graphpad.com).

3. Results and Discussion

SARS-CoV-2 has infected more than 442 million people and caused more than 6 million deaths worldwide, and the emergence of new variants has led to concerns regarding vaccine effectiveness. At the time of writing, alpha, beta, gamma, delta were the SARS-CoV-2 variants of concern (VOC) [35,51,52]. Additionally, the new VOC omicron is spreading rapidly, making it the predominant strain of SARS-CoV-2 in some countries [53]. Based on the above, the introduction of a new variant may decrease vaccine effectiveness, and a continued search for treatments is needed. We used computational approaches, such as docking and molecular dynamics simulation, to test FDA-approved drugs and identify potential candidates to treat COVID-19 by inhibiting the main proteins involved in the entry and replication process as shown in Table 1.

Table 1. Docking scores and binding-free energy calculations of the 15 best-ranked FDA-approved drugs against SARS-CoV-2 main protease (M^{pro}).

Compound ID	Traditional Name	FDA Status	Docking Score	$\Delta G_{(bind)}$ Kcal/mol	Biological Activity
DB00290	Bleomycin	Approved	−12.119	−96.63	Anticancer, antibiotic [54–57]
DB09487	Iotrolan	Approved	−13.411	−78.80	Radiocontrast agent [8]
DB01698	Troxerutin	Approved	−11.707	−83.08	Antioxidant, vasoprotective agent [58] SARS-CoV-2 M^{pro} [10]
DB06791	Lanreotide	Approved	−9.932	−65.15	Anticancer [59–61]
DB00803	Colistin	Approved	−11.315	−94.83	Antibiotic [62,63]
CHEMBL3989823	Viomycin Sulfate	Approved	−10.319	−74.63	Anti-tuberculosis, antibiotic [64]
DB01249	Iodixanol	Approved	−9.88	−91.33	Radiocontrast agent [8,65,66]
DB11672	Curcumin	Approved	−9.831	−70.24	Anti-inflammatory, hypoglycemic, antioxidant, and antimicrobial [54,67,68]
DB09134	Ioversol	Approved	−9.149	−44.95	Radiocontrast agent [66,69]
DB02638	Terlipressin	Approved	−8.513	−89.37	Hepatorenal syndrome, vasoactive drug in the management of hypotension [70]
DB00104	Octreotide	Approved	−8.21	−82.34	Anticancer [59,61]
DB01232	Saquinavir	Approved	−7.978	−64.49	HIV-1 protease inhibitor, inhibitor SARS-CoV-2 M^{pro} [71,72]
DB06240	Tariquidar	Approved	−7.224	−79.24	P-gp transporter inhibitor [73]
DB00007	Leuprolide	Approved	−6.406	125.56	Anticancer [74]

3.1. Drug Candidates May Inhibit the Viral Protein Translation

Different drugs have been previously predicted as M^{pro} inhibitors (Figure S2), where valrubicin, aprepitant, perphenazine, remdesivir, lopinavir, nelfinavir, bepotastine, and aloxistatin are included [5,75–77]. As shown in Table 1, our molecular docking suggests additional drugs that may inhibit the viral entry and inhibit the activity of SARS-CoV-2 main protease M^{pro}; within these drugs, biological actors, such as anticancer, antibiotic, anti-inflammatory, antioxidant, antiviral, and radiocontrast agents, are included. Our suggested M^{pro}'s inhibitor, viomycin, includes docking scores −10.319 and −74.63 Kcal/mol binding energy (Table 1). Additionally, molecular docking suggests a binding comprised of amino acid residues Thr 25—Leu 27, Phe 140—Cys 145, and His 163—Pro 168, with hydrogen bond interactions with relevant residues, such as Thr 25, Thr 26, Asn 142, Gly 143, Cys 145, and Glu 166 (Figure 1).

Even though the possible inhibitory effect of viomycin on M^{pro} was previously reported by Mahanta et al., 2022 [78], our docking results suggest an additional stronger interaction with residues Glu 166, Arg 188, and Gln 189, similar to those shown by N3 derivatives, which have higher inhibitory activity than N3 [18]. Its stability within the proposed binding pocket was further evaluated along the 100 ns of simulation by inspection of the root mean square deviation (RMSD) (Figure 2D). Molecular dynamics suggest stability within the proposed binding pocket along the simulation (Figure 2E), with protein–ligand interactions with relevant amino acid residues previously described by Jin et al., 2020 [18]. In this sense, viomycin is kept inside the binding pocket by having H-bond interactions with residues such as Glu 166 (almost 100% of simulation), Gln 189 (76% of the simulation),

Asn 142 (46% of the simulation), Ser46, and Glu 47, with 20% of interactions along the 100 ns (Figure 2A), where Gln 189 and Glu 186 are involved in substrate affinity [78]. Additionally, hydrogen bonds mediated by water (water bridges) are also present with residues Glu 166 (80% frequency), Gln 189 (60% of simulation), Asn 142 (40% of simulation), Thr 26, His 41, Glu 47, and Pro 168 (less than 40% frequency) along the 100 ns of simulation (Figure 2B). Finally, hydrophobic interactions with amino acid residue Pro 168 for 10% of the simulation are also included (Figure 2C).

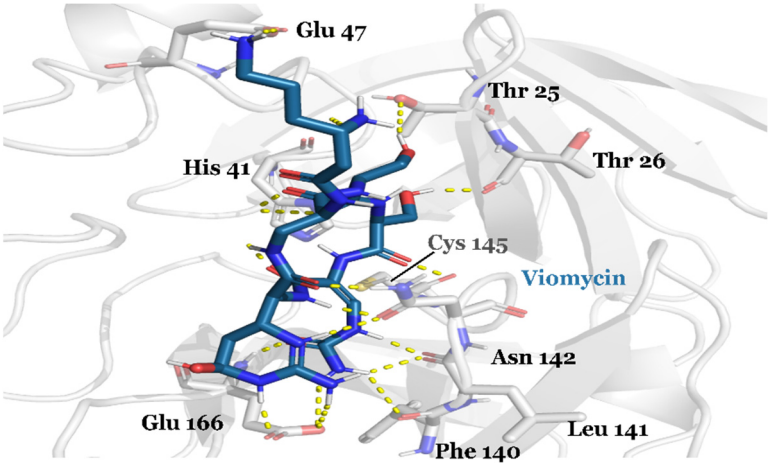

Figure 1. A representative snapshot of the docking pose of viomycin. M^{pro}'s residues are colored according to the atom type of the interacting amino acid residues (protein's carbon, light grey; oxygen, red; nitrogen, blue). The protein–ligand interactions are represented by dash lines as follows: hydrogen bond interactions are colored in yellow.

On the other hand, bleomycin (docking score of −12.119 and binding-free energy of −96.63 Kcal/mol), and lanreotide (a −9.932 docking score and binding-free energy −65.15 Kcal/mol) are also suggested as potential M^{pro} inhibitors (Table 1). Both are in a binding pocket consisting of residues Thr 24, Thr 26, His 41, and Glu 47 (Figure S3), with hydrogen bond interaction with the residues Thr 24, Thr 26, Asn 142, Gly 143, Gln 189, and Thr 190 also suggested by molecular docking (Figure S3). Bleomycin and lanreotide are anticancer compounds; some authors, such as Mafucci et al., 2020, and Chakraborti et al., 2020, have also reported bleomycin as a potential $M^{pro,}$ and S protein inhibitor, suggesting the strong urges for experimental testing of this peptidomimetic against SARS-CoV-2 [10,59,79]. However, the application in clinics of bleomycin has been limited due to its side effects, of which pulmonary fibrosis is considered the most severe [57,80].

Aside from the drugs mentioned above, inhibitors of HIV-protease, such as saquinavir, indinavir, and lopinavir, are also predicted as M^{pro} inhibitors (Table 1). These antiviral drugs have been tested to alleviate the mild-to-moderate SARS-CoV-2 symptoms in combination with ritonavir [34,81]. Additionally, radiocontrast agents, such as iodixanol and iotrolan, have been predicted as dual inhibitors by inhibiting M^{pro} and S protein activities (Tables 1 and 2). In this sense, iotrolan, one of the best-ranked M^{pro} inhibitors with a −13.411 docking score (Table 1), is in a pocket made up of amino acid residues Leu 141—Asp 187, His 164—Gly 170, and His 41—Met 49 (Figure S3E). Furthermore, the iodine substituents in the chemical structure of iotrolan are found by interacting with residues, such as His 41, Gln 189, and Leu 164. Authors have also reported radiocontrast agents, such as iotrolan and iodixanol, as potential M^{pro} inhibitors; however, these iodine-containing drugs carry significant limitations for their use in clinics due to their side effects; hypertensive reactions; and cardiovascular, ocular, and gastrointestinal complications [65,66]. Nevertheless, structural modifications in iotrolan and iodixanol could lead to safer antiviral agents, where modification in iodide groups with hydrogens could make them stable and safer as antivirals, although their affinity for M^{pro} could be compromised [8].

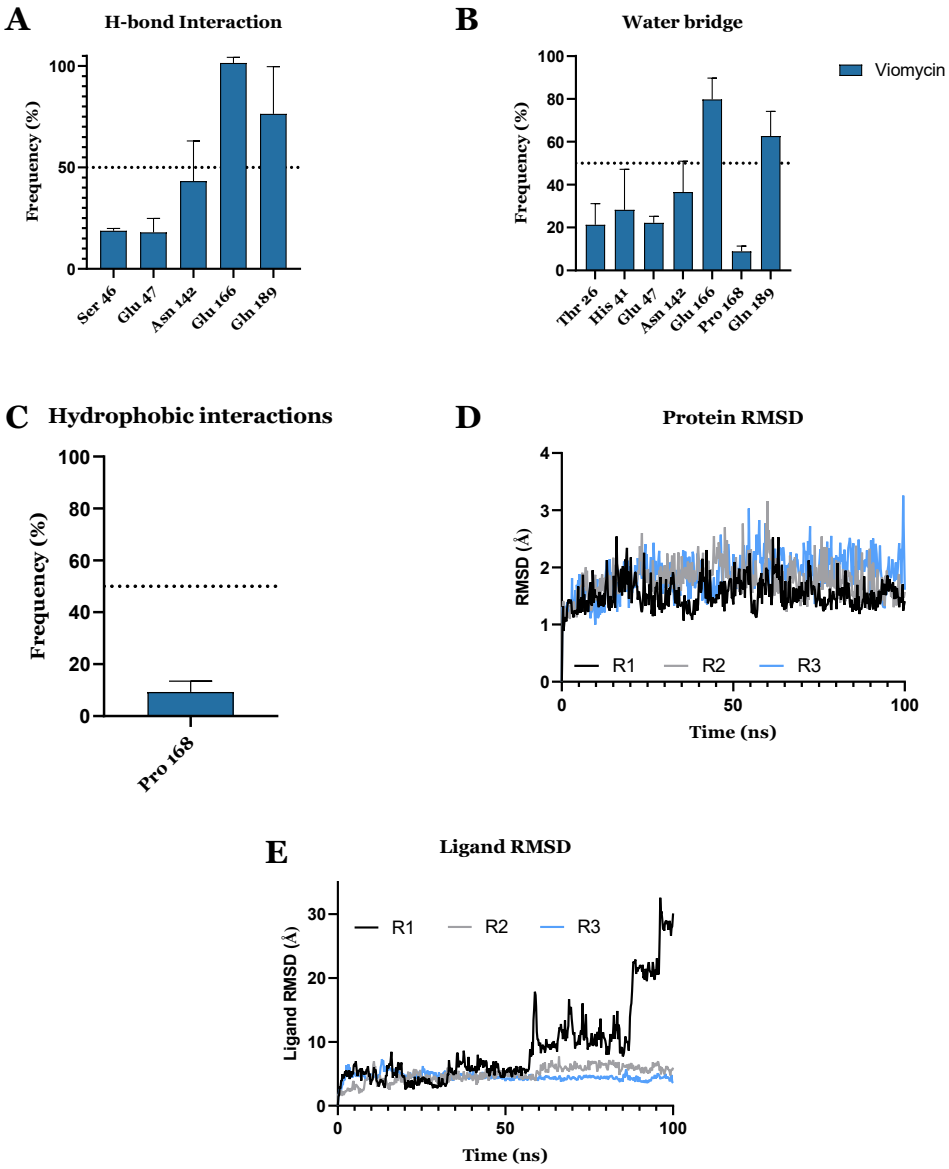

Figure 2. Viomycin protein–ligand interaction along the 100 ns simulation. Frequency of hydrogen bonding interactions (**A**); water-mediated hydrogen bonding interactions (**B**); hydrophobic interactions (**C**); representative picture of root mean square deviation (RMSD) values of protein backbone for the protein–viomycin complexes (**D**); ligand RMSD variation along the simulation time for viomycin (**E**).

Table 2. Docking scores and binding-free energy calculations of the 15 best-ranked FDA-approved drugs against SARS-CoV-2's the spike glycoprotein (S protein).

Compound ID	Traditional Name	FDA Status	Docking Score	$\Delta G_{(bind)}$ Kcal/mol	Activity
Site 1					
DB01362	Iohexol	Approved	−9.175	−58.99	Contrast agent [65]
DB04703	Hesperidin	Approved	−8.947	−66.09	Neuroprotective agent [82]
DB09487	Iotrolan	Approved	−8.313	−76.17	Radiocontrast agent [8]

Table 2. *Cont.*

Compound ID	Traditional Name	FDA Status	Docking Score	$\Delta G_{(bind)}$ Kcal/mol	Activity
DB09135	Ioxilan	Approved	−8.082	−62.37	Contrast agent [8]
DB14126	Tenofovir	Approved	−4.658	−46.10	Used to treat constipation [24], anti-ribonuclease H activity in HIV [83]
DB00811	Ribavirin	Approved	−5.117	−35.21	Antiviral agent [34]
DB00787	Acyclovir	Approved	−5.088	−46.10	Nucleotide analog antiviral used to treat herpes simplex [84]
			Site 2		
DB15617	Ferric derisomaltose	Approved	−10.192	−30.76	Used to treat iron-deficiency anemia [85]
DB09487	Iotrolan	Approved	−10.047	−60.03	Radiocontrast agent [8]
DB01362	Iohexol	Approved	−8.431	−57.64	Contrast agent [8]
DB12301	Doravirine	Approved	−8.199	−49.40	Used to treat HIV-1 infection [86]
CHEMBL2368547	Senosside A	Approved	−8.677	−39.58	Used to treat constipation [87], anti-ribonuclease H activity in HIV [88]
CHEMBL1534	Riboflavin	Approved	−8.027	−59.09	Used to treat vitamin B2 deficiency [89]
CHEMBL1200455	Iohexol	Approved	−7.997	−43.54	Contrast agent [66]
			Site 3		
DB01249	Iodixanol	Approved	−10.49	−61.92	Radiocontrast agent [66]
DB15617	Ferric derisomaltosa	Approved	−9.852	−55.90	Used to treat iron deficiency anemia [85]

At the same time, antioxidant and anti-inflammatory drugs, such as troxerutin and curcumin, are also predicted as potential M^{pro} inhibitors by our molecular docking (Table 1). Troxerutin (−11.707 docking score and −83.08 Kcal/mol binding energy) and curcumin (−9.831 docking score and −70.24 Kcal/mol binding energy) (Table 1) are in a binding pocket consisting of amino acid residues Thr 25—Leu 27, His 163—His 172, and Arg 188—Gln 192 (Figure S3). Authors Islam et al., 2021, and Manoharan et al., 2020, have reported curcumin as a phytochemical with a potential inhibitory effect against SARS-CoV-2 M^{pro} and preventive measures against COVID-19 [67,90]. Furthermore, curcumin could exhibit a protective effect mediated by angiotensin II receptors (AT1R and AT2R). In this sense, upregulation of AT2R induces AT1R suppression, leading to angiotensin II-AT2R-mediated anti-inflammatory effects involved the inhibition of NF-κB activity and oxidative stress [67].

In the same way, molecular dynamics simulations suggest a strong interaction between viomycin and relevant residues located at the active site of SARS-CoV-2 M^{pro}. Authors have reported an active site made up of amino acid residues Thr 24, Thr 26, Leu 27, His 41, Cys 44, Met 49, Pro 52, Ser 139, Phe 140, Leu 141, Asn 142, Gly 143, His 164, Glu 166, His 172, Phe 181, Gln 189, Thr 190, Gln 192, and Glu 168 involved in the S4 subpocket formed at M^{pro} [16,91]. Mihiretie et al., 2021, report Gly 143 as the most attractive residue to form an H-bond with ligand and Glu 166, Cys 145, and His 163 [92]. Interestingly, molecular dynamics and docking results suggest an H-bond interaction and water bridges between viomycin with some of these relevant residues, such as Glu 166 (Figure 2A,B). Moreover,

some reported M^{pro} inhibitors interact with similar residues to viomycin. First, one widely reported inhibitor, the Michael acceptor inhibitor (known as N3) reported by Jin et al., 2020, is located inside the M^{pro} active site where the Sγ atom of Cys 145 forms a covalent bond with the Cβ atom of its vinyl group [18]. In their study, Jin et al., 2020, found the P1 fragment of N3 in the S1 sub-pocket having an H-bond with amino acid His 163, whereas the P3 fragment is solvent-exposed, while the P5 fragment is in contact with Pro 168, as well as residues 190–191. In this sense, viomycin could be a potent inhibitory activity since modifications of P3 fragments on N3 inhibitors looking to have a larger side chain are an excellent option to find an inhibitor of the main protease where new inhibitors N27 and H16, which have a larger side chain at P3 position with stronger interactions with residues Glu 166, Arg 188, and Gln 189, have higher inhibitory activity compared to N3 [92]. As with viomycin, different drugs have been reported as potential M^{pro} inhibitors with similar protein–ligand interactions, where the neuromuscular blocking agent metocurine was reported in the substrate-binding pocket of the protease, having interactions with the amino acid residues Phe 140, Leu 141, Cys 145, His 163, His 164, Met 165, Glu 166, Leu 167, and Pro 168 [93].

Similarly, protease inhibitors boceprevir, narlaprevir, and telaprevir showed a specific binding against the main protease of SARS-CoV-2 where boceprevir through molecular docking showed H-bond interactions, as well as hydrophobic interactions, with critical residues His 41, Leu 141, His 164, Met 165, Glu 166, and Asp 187 [92]. In addition to the previously reported inhibitors, the protease inhibitors used to treat HIV nelfinavir, lopinavir, and ritonavir have effectively suppressed SARS-CoV through the inactivation of the M^{pro} where Thr 24, Thr 26, and Asn 119 are the critical residues for binding [92,94]. Altogether, docking results and molecular dynamics simulations against the main protease of SARS-CoV-2 suggest a potential inhibitory effect on M^{pro} since protein–ligand interactions with relevant residues involved in protease activity are present along the 100 ns. H-bond interactions, as well as hydrophobic interactions between viomycin and key amino acid residues such as Glu 166, Gln 189, Thr 24, and Thr 26, are also present within suggested drugs, such as remdesivir, narlaprevir, boceprevir, and nelfinavir, among others.

3.2. Drug Candidates May Inhibit SARS-CoV-2 Entry into the Host Cells

Like M^{pro}, the spike glycoprotein (S protein) is essential for viral entry into a host cell and is one of the main targets for drug design to fight COVID-19. As mentioned before, the subunit S1 of the functional subunits of S protein comprises the receptor-binding domain (RBD) and interacts directly with the host cell receptor. For this, the RBD region was used to evaluate the potential affinity between FDA-approved drugs and the S protein. As shown in Figure 3, three different grids were evaluated between the viral S protein and ACE2 receptor interface. The hydrophilic region (grid 1) is comprised of the key amino acid residues Gln 498, Thr 500, and Asn 501, while grid 2 is comprised of Lys 417 and Tyr 453. Finally, grid 3 is comprised of Gln 474, Phe 486, and Asn 487.

Our docking analysis suggests hesperidin within the top-ranked FDA-approved drugs against the S protein (Table 2). Hesperidin (docking score: −8.947; −66.09 Kcal/mol Table 2) is located near residues Gln 493—Tyr 505, making hydrogen bond interactions with residues Arg 403, Tyr 453, Ser 494, Gly 496, Gln 498, and Thr 500, as well as a π-π interaction with residue Tyr 505 (Figure 4).

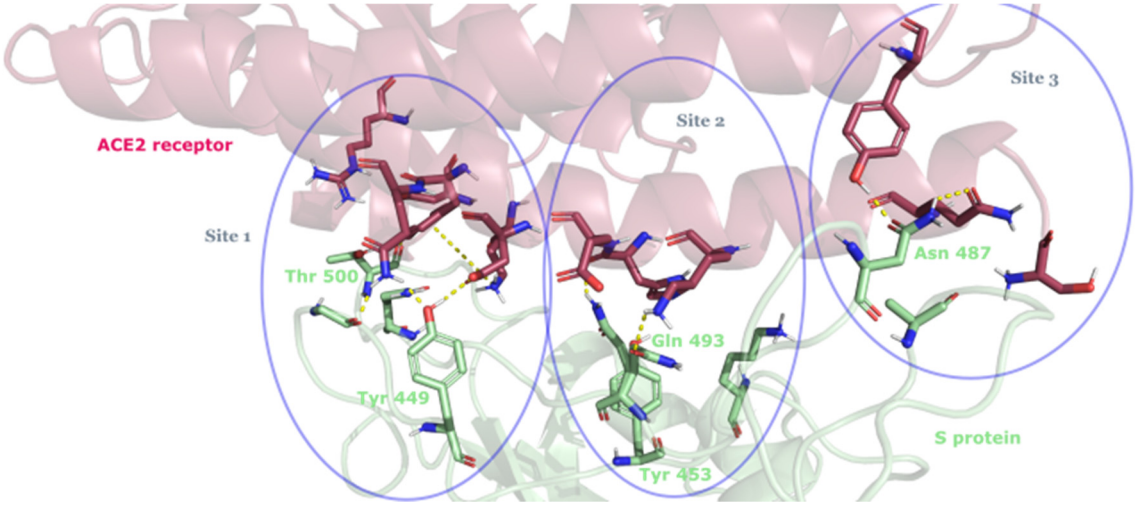

Figure 3. The interface between the viral S protein and ACE2 host cell receptor. Residues are colored according to the atom type of the interacting amino acid residues (the S protein's carbon, pale green; the ACE2 receptor's carbon, red; oxygen, red; nitrogen, blue). Dash lines represent the protein–ligand interactions: hydrogen bond interactions are colored in yellow. Figure adapted from Unni et al., 2020.

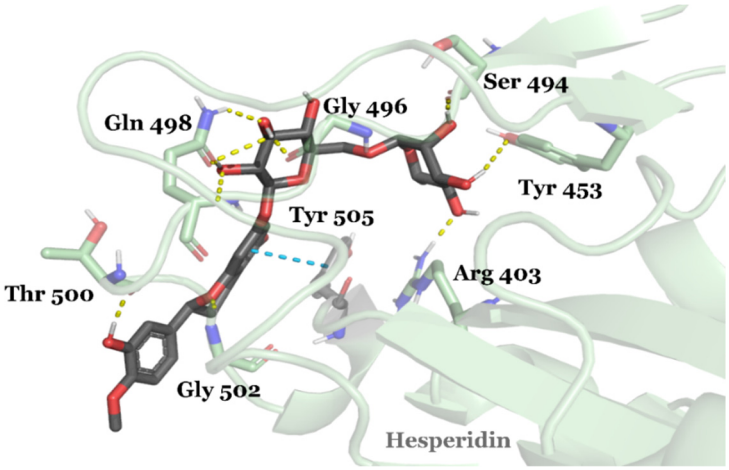

Figure 4. A representative snapshot of the docking pose of hesperidin. The S protein's residues are colored according to the atom type of the interacting amino acid residues (protein's carbon, pale green; oxygen, red; nitrogen, blue). Dash lines represent the protein–ligand interactions: hydrogen bond interactions are colored in yellow; π-π interactions are colored in blue.

Due to hesperidin interacting with relevant residues involved in SARS-CoV-2 infection mediated by interaction with the ACE2 and TMPRSS2 receptors, as shown by Cheng et al., 2021 [95], we evaluated the hesperidin stability in the proposed pocket by molecular dynamics simulation. Molecular dynamics simulation results show protein–ligand stability along the simulation time (Figure 5E,F), with a ligand fluctuation within the proposed pocket suggesting a possible conformation or ligand states (Figure 5F) without leaving the pocket.

Regarding interactions along the simulation, hesperidin makes H-bond interactions with residues such as Ser 494, Tyr 453, Gly 496, Asn 501, and Gly 502 with almost 40%, 35%, 36%, 35%, and 30% frequency, respectively (Figure 5A). In addition, water bridges are included between hesperidin and residues Asn 501 (35% frequency) and Arg 403 (20% frequency) (Figure 5B). Finally, hydrophobic interaction and π-π interaction with the amino acid residue are included with 15% and 35% frequency, respectively (Figure 5C,D).

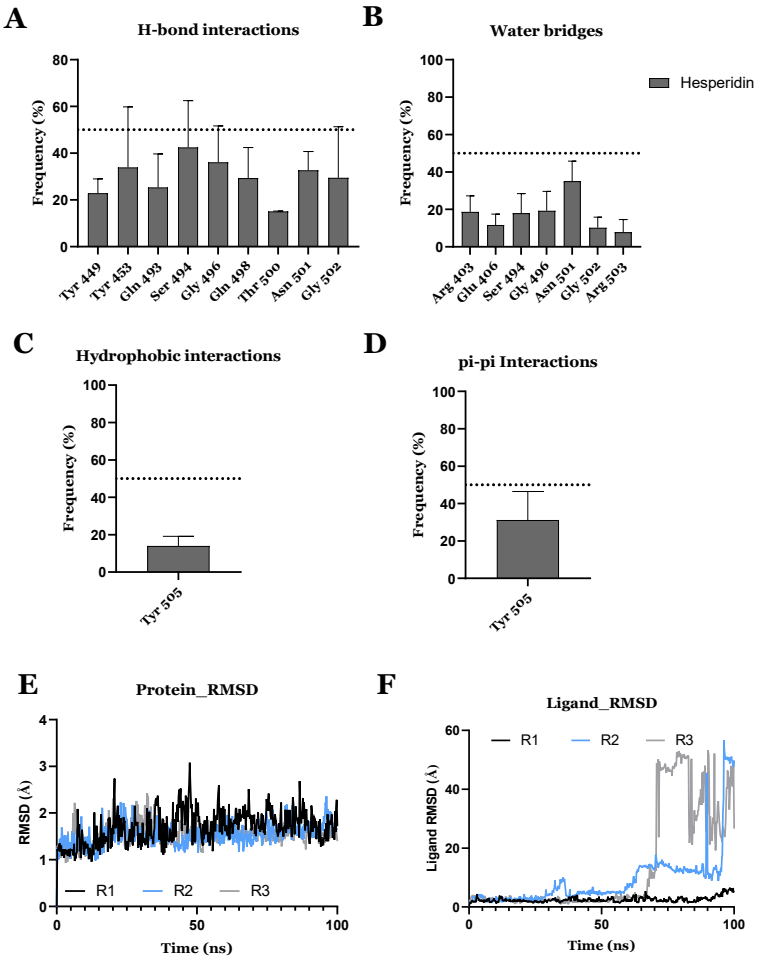

Figure 5. Hesperidin protein–ligand interaction along the 100 ns simulation. Frequency of hydrogen bonding interactions (**A**); water-mediated hydrogen bonding interactions (**B**); hydrophobic interactions (**C**); π-π interactions (**D**); representative picture of root mean square deviation (RMSD) values of protein backbone for the protein–hesperidin complexes (**E**); Ligand RMSD variation along the simulation time for viomycin (**F**).

As shown in Table 2, molecular docking suggests additional FDA-approved drugs that may inhibit SARS-CoV-2 entry into the host cell by interacting with relevant residues in the RDB of the S protein. Radiocontrast agents such as iohexol (Docking score, −9.175), iotrolan (Docking score, −8.313), and ioxilan (Docking score, −8.082) are included (Figure S4). However, as mentioned above, chemical modifications are needed to enhance their stability and safety and decrease their possible side effects [8]. Docking poses suggest a possible interruption between the S protein and ACE2 receptor by the abovementioned contrast agents, since Unni et al., 2020, hypothesized that H-bond interaction with residue Gly 496 and hydrophobic interaction with residue Tyr 505 may be able to break the site 1 interactions with the ACE2 receptor, specifically the interaction with residue Lys 343 [13].

Our docking results coincide with some authors, suggesting acyclovir as a potential drug against SARS-CoV-2 [96]. Acyclovir is in the hydrophobic cleft and the hook region of site 2, making interactions with residues such as Tyr 453, Arg 403, and near residue Glu 406 (Figure S4A). Additionally, π-π stacking with residue Tyr 495 and hydrophobic interaction with residue Tyr 505 may disrupt the S protein interaction with the ACE2 receptor [13]. Peters et al., 2015, demonstrated that acyclovir and its nucleoside analogs based on its acyclic sugar scaffold showed potential antiviral effects against MERS with EC_{50} and CC_{50} of 23 and 71 μM, respectively [97]. However, no suggested mechanisms, by which these analogs and their precursor, acyclovir, impair viral replication [96].

Moreover, antivirals ribavirin and tenofovir are also predicted by molecular docking (Table 2). H-bond interactions with residues Asn 501, Gly 496, Ser 494, and Glu 406 are included, as well as π-π interaction with Tyr 505 (Figure S4E,F). In this sense, as with previous reports, our docking results suggest potential S protein inhibition by ribavirin and tenofovir. Moreover, ribavirin downregulates the TMPR22 and decreases the ACE2 expression in infected Vero E6 cells after 48 h of treatment at 25 μM with no changes in Caco-2 cells [98]. Furthermore, some reports suggest that tenofovir or tenofovir/emtricitabine may reduce the SARS-CoV-2 viral load after day 7 compared to standard care. In this case, PrEP users who tested positive for SARS-CoV-2 showed twice as much asymptomatic infection as non-PrEP users [98,99]. However, there are also risks of HIV resistance if tenofovir becomes an experimental therapy for COVID-19. For that, the use of tenofovir outside of trials is not recommended but rather should be considered for inclusion in other generic antiviral therapies in multiarmed therapeutic trials.

Despite vaccination programs, COVID-19 infections are increasing due to different SARS-CoV-2 variants, such as B.1.617.2 (Delta). Delta lineage was identified in October 2020 in India with a high infection rate, which, according to the Centers for Disease Control and Prevention (CDC), caused between 80% and 87% of all U.S. COVID-19 cases in the last two weeks of July 2021 [35]. Therefore, it is necessary to continue searching for drugs and alternatives in the fight against these new variants. For that reason, we screened our database against the SARS-CoV-2 variants B.1.1.7 (Alpha) and its mutations within RBD in the S protein (Asn501Tyr) [100]; B.1.351 (Beta) Lys417Asn, Glu484Lys, Asn501Tyr; P.1 (Gamma) Lys417Thr, Glu484Lys, Asn501Tyr; and B.1.617.2 (Delta) Leu452Arg, Thr478Lys [101,102]. We aimed to identify the possible binding affinity of hesperidin as our previously selected drug in RBD in the S protein, as well as potential drugs against these new variants.

Our docking results in the B.1.1.7 (Alpha) variant show that hesperidin (docking score −6.284, −66.44 Kcal/mol, Table S1) is located in a pocket made up of residues Gly 498—Tyr 505. Additionally, H-bond interactions with residues Gln 498, Gly 502, and Tyr 505 are present, as well as π-π interactions with residues Tyr 501 and Tyr 505 (Figure 6). As with hesperidin, different FDA-approved drugs are included within the best-ranked compounds in the Alpha variant (Table S1). The oxytocin receptor agonist atosiban (docking score −5.204; −66.43 Kcal/mol Table S1), a gastrin-like molecule; pentagastrin (docking score −6.680; −62.36 Kcal/mol Table S1); protokylol (docking score −5.577; −57.85 Kcal/mol), a β-adrenergic receptor agonist; and iopamidol are also included in top-ranked FDA-approved drugs against the Alpha variant (Figure S5).

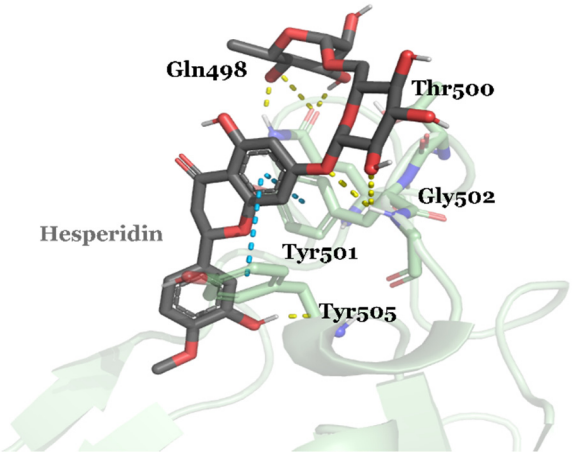

Figure 6. A representative snapshot of the docking pose of hesperidin with the Alpha variant. B.1.1.7 (Alpha's) residues are colored according to the atom type of the interacting amino acid residues (protein's carbon, pale green; oxygen, red; nitrogen, blue). Dash lines represent the protein–ligand interactions: hydrogen bond interactions are colored in yellow; π-π interactions are colored in blue.

Similarly, hesperidin (docking score −6.516; −65.70 Kcal/mol Table S2) in the B.1.351 (Beta) variant is located in a pocket comprised of residues Gln 498—Gly 502, making H-bond interactions with the residues Thr 500, Gln 498, and Gly 502 and π-π interactions with residues Tyr 501 and Tyr 505, as well as π- cation interactions with the residue Arg 403 (Figure 7). Different FDA-approved drugs with a wide range of biological activities, such as the HIV-inhibitor ritonavir; the contrast agents iotrolan, ioversol; and the prostaglandin reductase activity rutin, are included among the best-ranked drugs against this variant (Figure S6, Table S2). Regarding the B.1.617.2 (Delta) variant, our docking results suggest that hesperidin makes an H-bond interaction with residues Tyr 505, Gly 502, Tyr 501, Gln 498, and Thr 500 (Figure 8). Likewise, the anticancer drug goserelin, the antibiotic colistin, the anticancer lanreotide, and the contrast agents iodixanol and ioproline are included among the best-ranked compounds against this SARS-CoV-2 variant (Table S3).

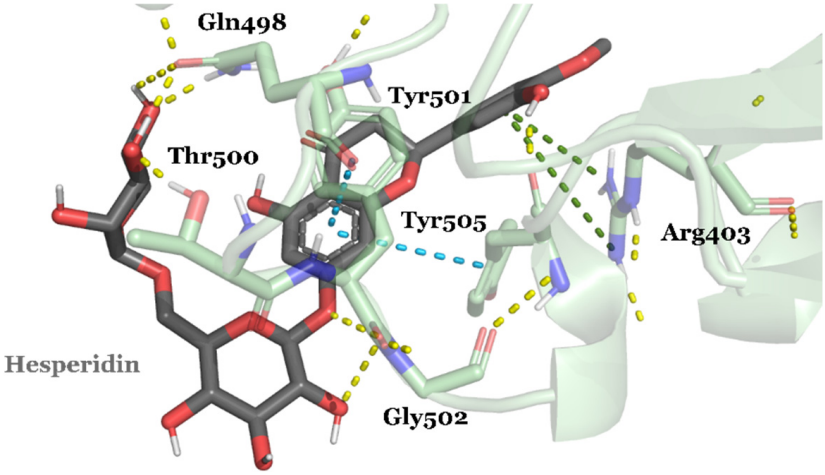

Figure 7. A representative snapshot of the docking pose of hesperidin with the Beta variant. B.1.351 (Beta's) residues are colored according to the atom type of the interacting amino acid residues (protein's carbon, pale green; oxygen, red; nitrogen, blue). Dash lines represent the protein–ligand interactions: hydrogen bond interactions are colored in yellow; π-π interactions are colored in blue; π-cation interactions are colored in green.

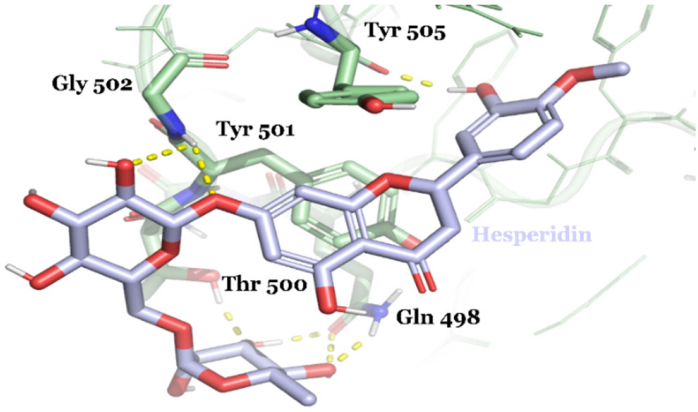

Figure 8. A representative snapshot of the docking pose of hesperidin with the Delta variant. B.1.617.2 (Delta's) residues are colored according to the atom type of the interacting amino acid residues (protein's carbon, pale green; oxygen, red; nitrogen, blue). Dash lines represent the protein–ligand interactions: hydrogen bond interactions are colored in yellow; π-π interactions are colored in blue; π-cation interactions are colored in green.

It is well known that the interaction between the RBD region of the S protein and ACE2 plays a crucial role in their binding affinity following the viral infection [38]. In

this sense, our docking result, as well as our molecular dynamics simulations, suggest a possible decrease in the S protein/ACE2 interactions mediated by hesperidin due to H-bond interactions with key residues involved in a viral entry within the host cell (Figure 4). Relevant residues included within the receptor-binding motif (RBM)Leu 455 and Gln 493 are reported to have favorable interactions with the ACE2 residues Lys 31 and Glu 35, respectively [103]. Furthermore, hesperidin interaction with the critical residue Gln 498 (Figures 4 and 5A,B) might decrease the H-bond interactions between the S protein and residue Tyr 41 of ACE2, where molecular docking shows that the substitution of SARS-CoV-2 Gln 498 with Tyr 484 forms π-π interactions with the same ACE2 residue, which explains the enhanced ACE2 binding [103,104]. Moreover, hesperidin also makes an H-bond interaction and water bridge with relevant residue Asn 501 (Figure 9A,C). Structural data suggest that Asn 501 has a strong interaction with the ACE2 residue Lys 353, and its mutation with Thr 501 can stabilize the overall RBD structure through hydrophilic interactions enhancing its binding with ACE2 [35,38]. Additionally, the present study highlights the potential use of hesperidin against SARS-CoV-2 variants of concern (VOC) since these variants have been demonstrated to increase transmissibility, increase disease severity, and have a significant impact on treatments, as they decrease the neutralization activity of antibodies produced by vaccines [105,106]. These variants have several mutations within the receptor-binding domain (RBD) in the spike glycoprotein that may enhance the affinity of the S protein for ACE2. Mutations such as L452R, E484K, and N501Y included in some VOCs are located within the receptor-binding motif and directly comprise the interaction with the ACE2 receptor [107]. Our docking results suggest that hesperidin may disrupt the interaction between the S protein and ACE2 receptor through its π-π interactions between its aromatic ring and the N501Y mutation included in the Alpha, Beta, and Delta variants (Figures 6–8). These results are interesting since the N501Y mutation increases the ACE2 binding affinity, and this enhancement was preserved in combination with the mutations D614G and E484K [107]. These results are in concordance with the results obtained by Cheng et al., 2021, where hesperidin decreases SARS-CoV-2 infection by inhibiting the ACE2 receptor and TMPRS2 [95]. These results show that hesperidin may modulate the affinity between the S protein and ACE2 receptor since increased ACE2 affinity is mainly driven by the N501Y mutation.

In this sense, hesperidin interactions with Asn 501 might decrease the interaction between SARS-CoV-2 and ACE2. At the same time, the Asn 501 mutation found in the B.1.617.2, B.1.1.7, and B.1.351 (Beta) variants with Tyr 501 could stabilize its interaction by making π-π stacking interactions with hesperidin (Figures 6–8). Overall, hesperidin may decrease SARS-CoV-2 infection by diminishing the interactions between the S protein and ACE2 due to its interactions with relevant residues, such as Asn 439, Leu 452, Thr 470, Glu 484, Gln 498, and Asn 501. These residues are reported as critical for SARS-CoV-2 binding to ACE2 and can increase the infectibility of natural RBD mutations during virus transmission.

3.3. FDA-Approved Drug Candidates May Inhibit SARS-CoV-2 Replication

The third evaluated target in this work, the RdRp complex, is used for the SARS-CoV-2 virus for the replication of its genome and the transcription of its genes [108]. As shown in Table 3, we identified several interactions between FDA-approved drugs and RdRp that seem relevant for effective binding. Six antiviral drugs hit the top of our ranking: inarigivir, cidofovir, zanamivir, faldaprevir, elvitegravir, and ribavirin. Four antibiotics were identified as potential RdRp inhibitors: demeclocycline, nystatin, ticarcillin, and latamoxef. Additionally, radiocontrast agents mangafodipir and iotrolan were also found to be potential RdRp inhibitors (Table 3).

Table 3. Docking scores and binding-free energy calculations of the best-ranked FDA-approved drugs against RNA-dependent RNA polymerase (RdRp).

Compound ID	Traditional Name	FDA Status	Docking Score	$\Delta G_{(bind)}$ Kcal/mol	Activity
DB00618	Demeclocycline	Approved	−14.225	−2.73	Antibiotic, also is used to treat hyponatremia [109]
DB11365	Sennoside	Research	−14.040	−47.94	Used to treat constipation [24]
DB06796	Mangafodipir	Approved	−13.433	−31.72	Contrast agent
DB00650	Leucovorin	Approved	−13.424	−0.07	Used to prevent toxic effects after high-dose methotrexate therapy
DB11596	Levoleucovorin	Approved	−13.322	−7.54	Used to prevent toxic effects after high-dose methotrexate therapy
DB00923	Ceforanide	Approved	−12.969	63.36	Antibacterial activity
DB09487	Iotrolan	Approved	−12.951	6.25	Radiocontrast agent [5]
DB15062	Inarigivir	Research	−11.882	−1.37	Used to treat hepatitis B virus
DB00646	Nystatin	Approved	−11.669	−60.13	Antifungal activity
DB01076	Atorvastatin	Approved	−11.117	39.19	Antilipemic agent
DB01607	Ticarcillin	Approved	−11.095	−34.52	Antibiotic
DB00369	Cidofovir	Approved	−10.972	32.78	Antiviral activity against human cytomegalovirus
DB06794	Lodoxamide	Approved	−10.967	7.96	Ophthalmic agent
DB00558	Zanamivir	Approved	−10.869	90.24	Used to treat influenza viruses A and B
DB04570	Latamoxef	Approved	−10.843	24.25	Antibiotic used against Gram-positive and Gram-negative bacteria
DB11808	Faldaprevir	Research	−10.750	45.70	Antiviral agent against hepatitis C virus
DB09292	Sacubitril	Approved	−10.650	7.38	Used to treat cardiovascular diseases
DB09101	Elvitegravir	Approved	−10.432	−34.56	HIV-1 treatment
DB14663	Ribavirin monophosphate	Approved	−9.075	−19.72	Antiviral agent against hepatitis C virus

The antifungal nystatin, used to treat mycotic infections, particularly those caused by the *Candida* species (docking score, −11.669; −60.13 Kcal/mol, Table 3), is located in a pocket formed by residues Ser 682—Asn 691 and Lys 551—Lys 545, making hydrogen bond interactions with residues Asn 496, Lys 545, Ser 549, Ser 814, Ser 759, Ala 688, and Ala 685 (Figure 10). Molecular dynamics simulation was used to evaluate the nystatin stability within the proposed binding pocket, suggesting nystatin stability inside the pocket (Figure S7) mediated by strong H-bond interactions with residues Ala 688 and Ser 814 with 40 and 80% frequency, respectively (Figure 9A). Hydrogen bond interactions mediated by water are also included with Asp 623 and Ser 759 with almost 40% frequency (Figure 9C). Finally, ionic interactions generated by the Mg ions at the RdRp catalytic site and charged residues are present along the 100 ns simulation between nystatin and Asp 618, Asp 760, Asp 761, and Asp Glu 811 (Figure 9D).

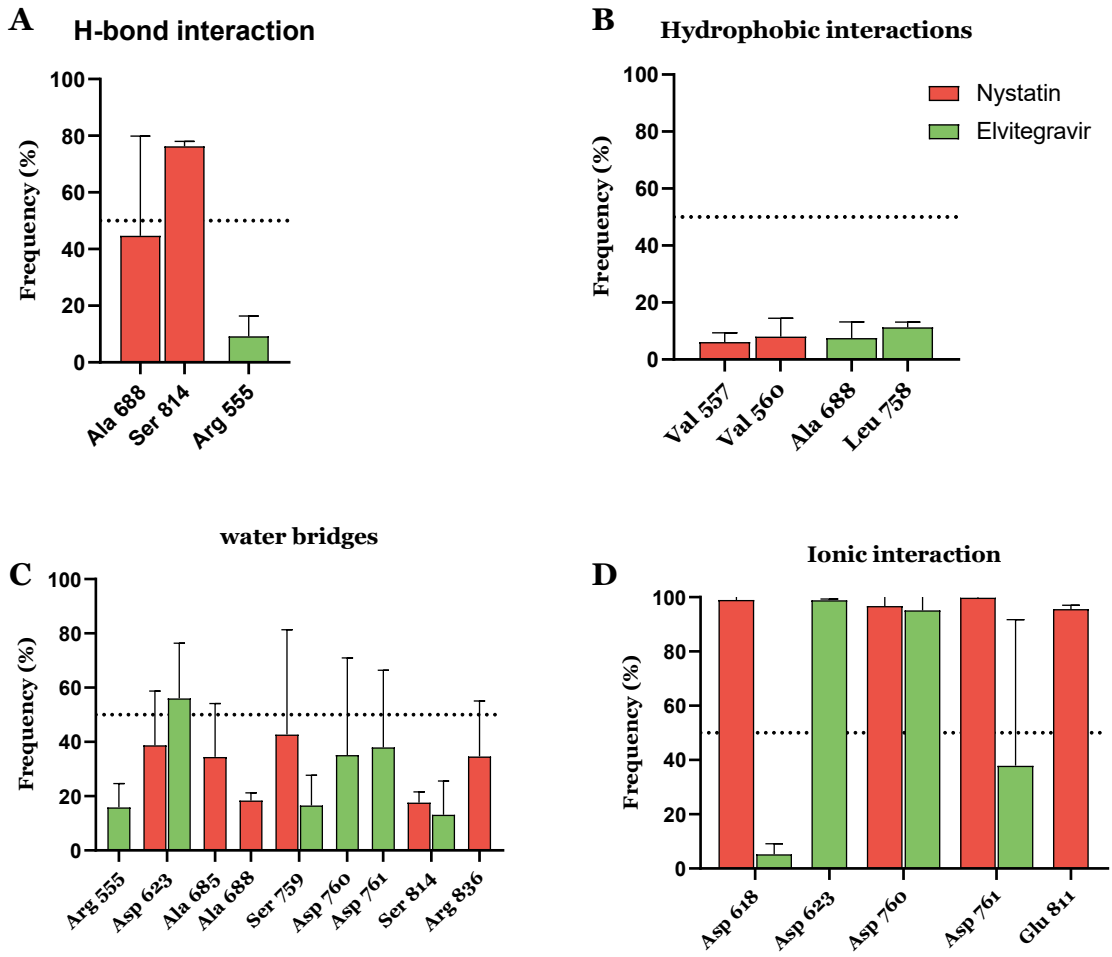

Figure 9. Nystatin and elvitegravir protein–ligand interaction along the 100 ns simulation. Frequency of hydrogen bonding interactions (**A**); hydrophobic interactions (**B**); water-mediated hydrogen bonding interactions (**C**); ionic interactions (**D**).

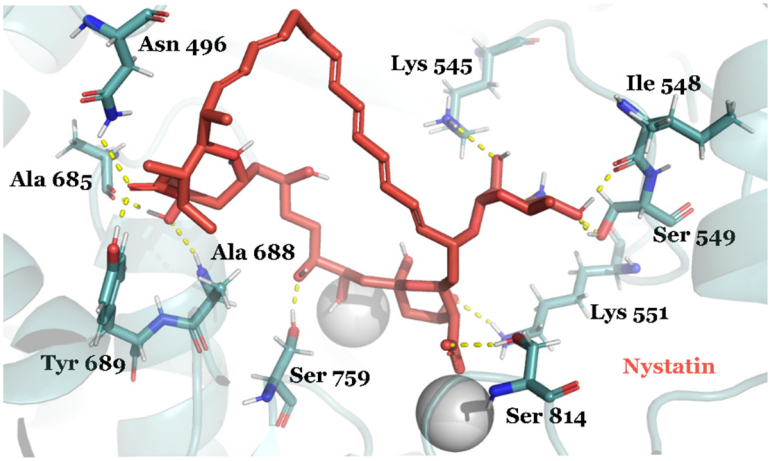

Figure 10. Nystatin-selected docking pose. RdRp's residues are colored according to the atom type of the interacting amino acid residues (protein's carbon, light teal; oxygen, red; nitrogen, blue). Dash lines represent the protein–ligand interactions: hydrogen bond interactions are colored in yellow; π-π interactions are colored in blue.

At the same time, the stability inside the predicted pocket of antiretroviral elvitegravir (docking score −10.432; −34.56 Kcal/mol, Table 3) used for the treatment of HIV-1 infection

was also simulated (Figure 11). Elvitegravir remains stable inside the pocket mediated by ionic interactions between elvitegravir, Mg ions, and residues Asp 623, Asp 760, and Asp761 with 100%, 100%, and 40% frequency (Figure 11). Additionally, water bridges with key residues, such as Asp 623, Asp 760, and Asp 761 (50%, 40%, and 40%, respectively Figure 9C) are also included, as well as H-bond interaction with Arg 555 (20% frequency, Figure 9A).

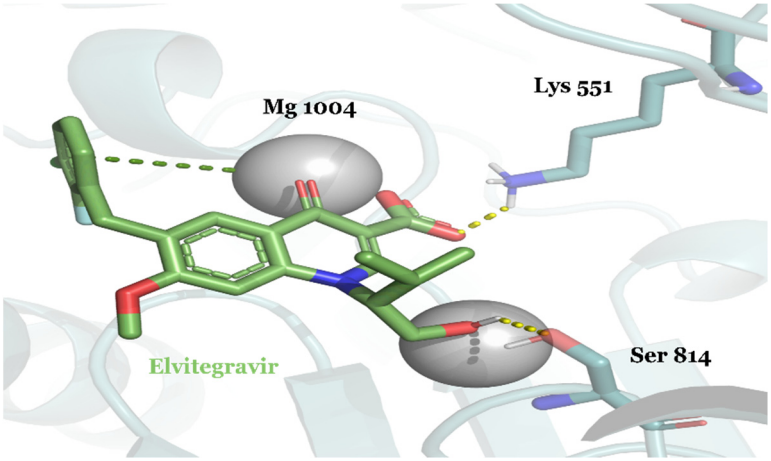

Figure 11. Elvitegravir-selected docking pose. RdRp's residues are colored according to the atom type of the interacting amino acid residues (protein's carbon, light teal; oxygen, red; nitrogen, blue). Dash lines represent the protein–ligand interactions: hydrogen bond interactions are colored in yellow; π-π interactions are colored in blue; π-cation interactions are colored in green.

Besides nystatin and elvitegravir, our docking results suggest as potential RdRp inhibitors demeclocycline (docking score, −14.225; −2.73 Kcal/mol, Table 3); leucovorin (docking score, −13.424; −0.07 Kcal/mol, Table 3); and levoleucovorin (docking score −13.322; −7.54 Kcal/mol, Table 3), located in a pocket comprised of residues Lys 551—Ala 558, Arg 624—Tyr 619, and Ser 682—Thr 680 (Figure S8). Additionally, radiocontrast agents mangafodipir and iotrolan are also suggested as potential RdRp inhibitors (Table 3). Mangafodipir (docking score, −13.433; −31.72 Kcal/mol, Table 3) and iotrolan (docking score, −12.959; 6.25 Kcal/mol, Table 3) are in a pocket formed by residues Ser 549—Arg 555, and Asp 618—Lys 621, making H-bond interactions with residues Lys 545, Arg 555, Lys 621, Ser 549, and Arg 836 (Figure S8). Additionally, halogen interactions between iodide atoms and residues Ser 814 and Tyr 689 stabilize their position within the predicted binding site.

Docking results and molecular dynamics simulations suggest that nystatin and elvitegravir may inhibit the SARS-CoV-2 RdRp polymerase due to their stability within the proposed binding pocket (Figure S7), which is characterized by strong binding pocket ionic interactions with key residues (Figure 9D). In the search for drugs for COVID-19 treatment, different antiviral drugs have been identified by targeting key proteins involved in different life cycle stages of SARS-CoV-2, and some of them are now in the clinical trial stage [43]. The antiviral drug remdesivir is one of the main RdRp inhibitors, positioned at the center of the catalytic site, forming stacking interactions and two hydrogen bonds with the purine base from the RNA template. Additionally, remdesivir makes hydrogen bond interactions with the side chain residues Lys 545 and Arg 555 [14]. Furthermore, key residues involved in remdesivir binding include Arg 553, Val 557, Asp 618, Ser 623, Thr 680, Asp 682, Gln 691, Asp 760, and Asp 761 [110]. Recently, Kabinger et al., 2021, showed that molnupiravir induces RNA mutagenesis since RdRp uses the active form of molnupiravir as a substrate instead of cytidine or uridine triphosphate [111,112]. Therefore, our results suggest that nystatin and elvitegravir may inhibit SARS-CoV-2 RdRp mediated by their interactions with relevant residues and their position within the protein-active site (Figures 10 and 11).

In this sense, nystatin and elvitegravir have ionic interactions with Asp 760 and Asp 761 (Figure 9D) involved in the Mg coordination, including in the RdRp palm subdomain, forming the catalytic site [113]. Additionally, elvitegravir makes H-bond interaction with residue Arg 555 (included in the motif F), an important residue involved in the interaction with the primer strand RNA, stabilizing the incoming nucleotide in the correct position for catalysis [14]. In this sense, since Arg 555 and Lys 545 make an H-bond interaction with the primer strand, the interaction between elvitegravir and Arg 555 may explain the possible elvitegravir inhibitory effect.

4. Conclusions

Our docking and molecular dynamics simulations provide new insights about the possible drug repurposing of viomycin (interacting with M^{pro}) and its interactions with key residues, such as Asn 143, Glu 166, and Gln 189, elvitegravir, and nystatin (interacting with RdRp). Their interactions with residues Asp 760, Asp 761, and Asp 618 may be able to inhibit the viral life cycle of SARS-CoV-2. Here, we also show hesperidin interaction with residue Tyr 501, a conserved amino acid in the S protein of different SARS-CoV-2 variants, decreasing the affinity between the S protein and ACE2 receptor, suggesting it as a good candidate to block the infection from the Alpha, Beta, and Delta VOCs.

Aside from the above-mentioned drugs, several iodide-based contrast agents (i.e., iohexol (−58.99 Kcal/mol), iotrolan (−76.19 Kcal/mol), and ioxilan (−62.37 Kcal/mol)) were also found to bind the defined binding sites of the S protein strongly (Table 2). Although the information we report here is the possible strong interaction between these contrast agents and SARS-CoV-2's S protein, M^{pro}, and RdRp, we believe that further investigation including chemical modifications in their structures might bring relevant advances in COVID-19 treatment.

Supplementary Materials: The following supporting information can be downloaded at: https://www.mdpi.com/article/10.3390/scipharm90020024/s1. Figure S1: Surface representation of substrate-binding pocket in SARS-CoV-2 Mpro. Relevant amino acid residues, S1, S1', S2, and S4 subsites are indicated [18]; Figure S2: List of principal drugs previously predicted as Mpro inhibitors; Figure S3: Representative snapshots of the docking pose of best ranked FDA-approved drugs in-teracting in Mpro; Figure S4: Representative snapshots of the docking poses of best ranked FDA-approved drug in S protein; Figure S5: Representative snapshots of the docking poses of best ranked FDA-approved drug in B.1.1.7 (Alpha) variant; Figure S6: Representative snapshots of the docking poses of best ranked FDA-approved drug in B.1.351 (Beta) variant; Figure S7: Repre-sentative picture of root mean square deviation (RMSD) values of protein backbone for the RdRp complexes; Figure S8: Representative snapshot of the docking poses best ranked compounds in RdRp; Table S1: Docking score and free binding energy calculation of best 15 ranked FDA-approved drugs against SARS-CoV-2 Spike glycoprotein (S-protein) B.1.1.7 (Alpha) variant [114–130]; Table S2: Docking score and free binding energy calculation of best 15 ranked FDA-approved drugs against SARS-CoV-2 Spike glycoprotein (S-protein) B.1.351 (Beta) variant [59,65,115,131–137]; Table S3: Docking score and free binding energy calculation of best 15 ranked FDA-approved drugs against SARS-CoV-2 Spike glycoprotein (S-protein) B.1.617.2 (Delta) variant [138–149].

Author Contributions: L.C.V., C.A.R.-H. and J.J.A.-J. contributed to the execution, analysis, data interpretation, and writing process. S.C.M.-S., J.E.D. and B.R.-O. contributed to the study design, analysis, interpretation of the data, and writing of the manuscript. All authors have read and agreed to the published version of the manuscript.

Funding: This project was supported by SGR Project BPIN: 2020000100126, Fortalecimiento de capacidades instaladas de CyT en el área de Epidemiología Molecular Virológica de la sede UIS-Guatiguará para aplicación de herramientas para atender problemáticas asociadas con patógenos de alto riesgo para la salud humana en Santander.

Institutional Review Board Statement: Not applicable.

Informed Consent Statement: Not applicable.

Data Availability Statement: Not applicable.

Acknowledgments: The authors want to thank the Ministerio de ciencias tecnología e innovación-Colciencias.

Conflicts of Interest: The authors declare no conflict of interest.

References

1. Salman, S.; Shah, F.H.; Idrees, J.; Idrees, F.; Velagala, S.; Ali, J.; Khan, A.A. Virtual screening of immunomodulatory medicinal compounds as promising anti-SARS-CoV-2 inhibitors. *Future Virol.* **2020**, *15*, 267–275. [CrossRef]
2. Li, Y.C.; Bai, W.Z.; Hashikawa, T. The neuroinvasive potential of SARS-CoV2 may play a role in the respiratory failure of COVID-19 patients. *J. Med. Virol.* **2020**, *92*, 552–555. [CrossRef] [PubMed]
3. Gu, J.; Han, B.; Wang, J. COVID-19: Gastrointestinal Manifestations and Potential Fecal-Oral Transmission. *Gastroenterology* **2020**, *158*, 1518–1519. [CrossRef] [PubMed]
4. Lau, S.K.P.; Li, K.S.M.; Tsang, A.K.L.; Lam, C.S.F.; Ahmed, S.; Chen, H.; Chan, K.-H.; Woo, P.C.Y.; Yuen, K.-Y. Genetic Characterization of Betacoronavirus Lineage C Viruses in Bats Reveals Marked Sequence Divergence in the Spike Protein of Pipistrellus Bat Coronavirus HKU5 in Japanese Pipistrelle: Implications for the Origin of the Novel Middle East Respiratory Sy. *J. Virol.* **2013**, *87*, 8638–8650. [CrossRef]
5. Yousefi, H.; Mashouri, L.; Okpechi, S.C.; Alahari, N. Repurposing existing drugs for the treatment of COVID-19/SARS-CoV-2 infection: A review describing drug mechanisms of action. *Biochem. Pharmacol.* **2021**, *183*, 114296. [CrossRef] [PubMed]
6. Sun, L.; Li, P.; Ju, X.; Rao, J.; Huang, W.; Ren, L.; Zhang, S.; Xiong, T.; Xu, K.; Zhou, X.; et al. In vivo structural characterization of the SARS-CoV-2 RNA genome identifies host proteins vulnerable to repurposed drugs. *Cell* **2021**, *184*, 1865–1883.e20. [CrossRef]
7. Wrapp, D.; Wang, N.; Corbett, K.S.; Goldsmith, J.A.; Hsieh, C.L.; Abiona, O.; Graham, B.S.; McLellan, J.S. Cryo-EM structure of the 2019-nCoV spike in the prefusion conformation. *Science* **2020**, *367*, 1260–1263. [CrossRef]
8. Kanhed, A.M.; Patel, D.V.; Teli, D.M.; Patel, N.R.; Chhabria, M.T.; Yadav, M.R. Identification of potential Mpro inhibitors for the treatment of COVID-19 by using systematic virtual screening approach. *Mol. Divers.* **2021**, *25*, 383–401. [CrossRef]
9. Tariq, A.; Mateen, R.M.; Afzal, M.S.; Saleem, M. Paromomycin: A potential dual targeted drug effectively inhibits both spike (S1) and main protease of COVID-19. *Int. J. Infect. Dis.* **2020**, *98*, 166–175. [CrossRef]
10. Kumar, P.; Bhardwaj, T.; Kumar, A.; Gehi, B.R.; Kapuganti, S.K.; Garg, N.; Nath, G.; Giri, R. Reprofiling of approved drugs against SARS-CoV-2 main protease: An in-silico study. *J. Biomol. Struct. Dyn.* **2020**, *40*, 3170–3184. [CrossRef]
11. Tsuji, M. Potential anti-SARS-CoV-2 drug candidates identified through virtual screening of the ChEMBL database for compounds that target the main coronavirus protease. *FEBS Open Bio.* **2020**, *10*, 995–1004. [CrossRef] [PubMed]
12. Xiao, X.; Chakraborti, S.; Dimitrov, A.S.; Gramatikoff, K.; Dimitrov, D.S. The SARS-CoV S glycoprotein: Expression and functional characterization. *Biochem. Biophys. Res. Commun.* **2003**, *312*, 1159–1164. [CrossRef] [PubMed]
13. Unni, S.; Aouti, S.; Thiyagarajan, S.; Padmanabhan, B. Identification of a repurposed drug as an inhibitor of Spike protein of human coronavirus SARS-CoV-2 by computational methods. *J. Biosci.* **2020**, *45*, 130. [CrossRef]
14. Yin, W.; Luan, X.; Li, Z.; Zhou, Z.; Wang, Q.; Gao, M.; Wang, X.; Zhou, F.; Shi, J.; You, E.; et al. Structural basis for inhibition of the SARS-CoV-2 RNA polymerase from SARS-CoV-2 by remdesivir. *Nat. Struct. Mol. Biol.* **2021**, *28*, 319–325. [CrossRef]
15. Liu, C.; Zhou, Q.; Li, Y.; Garner, L.V.; Watkins, S.P.; Carter, L.J.; Smoot, J.; Gregg, A.C.; Daniels, A.D.; Jervey, S.; et al. Research and Development on Therapeutic Agents and Vaccines for COVID-19 and Related Human Coronavirus Diseases. *ACS Cent. Sci.* **2020**, *6*, 315–331. [CrossRef] [PubMed]
16. Ekins, S.; Mottin, M.; Ramos, P.R.P.S.; Sousa, B.K.P.; Neves, B.J.; Foil, D.H.; Zorn, K.M.; Braga, R.C.; Coffee, M.; Southan, C.; et al. Déjà vu: Stimulating open drug discovery for SARS-CoV-2. *Drug Discov. Today* **2020**, *25*, 928–941. [CrossRef] [PubMed]
17. Tahir ul Qamar, M.; Alqahtani, S.M.; Alamri, M.A.; Chen, L.L. Structural basis of SARS-CoV-2 3CLpro and anti-COVID-19 drug discovery from medicinal plants. *J. Pharm. Anal.* **2020**, *10*, 313–319. [CrossRef] [PubMed]
18. Jin, Z.; Du, X.; Xu, Y.; Deng, Y.; Liu, M.; Zhao, Y.; Zhang, B.; Li, X.; Zhang, L.; Peng, C.; et al. Structure of Mpro from SARS-CoV-2 and discovery of its inhibitors. *Nature* **2020**, *582*, 289–293. [CrossRef] [PubMed]
19. Kim, Y.; Liu, H.; Galasiti Kankanamalage, A.C.; Weerasekara, S.; Hua, D.H.; Groutas, W.C.; Chang, K.O.; Pedersen, N.C. Reversal of the Progression of Fatal Coronavirus Infection in Cats by a Broad-Spectrum Coronavirus Protease Inhibitor. *PLoS Pathog.* **2016**, *12*, e1005531. [CrossRef]
20. Dai, W.; Zhang, B.; Jiang, X.M.; Su, H.; Li, J.; Zhao, Y.; Xie, X.; Jin, Z.; Peng, J.; Liu, F.; et al. Structure-based design of antiviral drug candidates targeting the SARS-CoV-2 main protease. *Science* **2020**, *368*, 1331–1335. [CrossRef]
21. Tortorici, M.A.; Veesler, D. Structural Insights into Coronavirus Entry. *Adv. Virus Res.* **2019**, *105*, 93–116. [CrossRef] [PubMed]
22. Zhou, P.; Yang, X.L.; Wang, X.G.; Hu, B.; Zhang, L.; Zhang, W.; Si, H.R.; Zhu, Y.; Li, B.; Huang, C.L.; et al. A pneumonia outbreak associated with a new coronavirus of probable bat origin. *Nature* **2020**, *579*, 270–273. [CrossRef] [PubMed]
23. Sungnak, W.; Huang, N.; Bécavin, C.; Berg, M.; Queen, R.; Litvinukova, M.; Talavera-López, C.; Maatz, H.; Reichart, D.; Sampaziotis, F.; et al. SARS-CoV-2 entry factors are highly expressed in nasal epithelial cells together with innate immune genes. *Nat. Med.* **2020**, *26*, 681–687. [CrossRef] [PubMed]

24. Hoffmann, M.; Kleine-Weber, H.; Schroeder, S.; Krüger, N.; Herrler, T.; Erichsen, S.; Schiergens, T.S.; Herrler, G.; Wu, N.H.; Nitsche, A.; et al. SARS-CoV-2 Cell Entry Depends on ACE2 and TMPRSS2 and Is Blocked by a Clinically Proven Protease Inhibitor. *Cell* **2020**, *181*, 271–280.e8. [CrossRef]
25. Wu, C.; Liu, Y.; Yang, Y.; Zhang, P.; Zhong, W.; Wang, Y.; Wang, Q.; Xu, Y.; Li, M.; Li, X.; et al. Analysis of therapeutic targets for SARS-CoV-2 and discovery of potential drugs by computational methods. *Acta Pharm. Sin. B* **2020**, *10*, 766–788. [CrossRef]
26. Ahn, D.G.; Choi, J.K.; Taylor, D.R.; Oh, J.W. Biochemical characterization of a recombinant SARS coronavirus nsp12 RNA-dependent RNA polymerase capable of copying viral RNA templates. *Arch. Virol.* **2012**, *157*, 2095–2104. [CrossRef]
27. Ziebuhr, J. The coronavirus replicase. *Curr. Top. Microbiol. Immunol.* **2005**, *287*, 57–94. [CrossRef]
28. Gao, Y.; Yan, L.; Huang, Y.; Liu, F.; Zhao, Y.; Cao, L.; Wang, T.; Sun, Q.; Ming, Z.; Zhang, L.; et al. Structure of the RNA-dependent RNA polymerase from COVID-19 virus. *Science* **2020**, *368*, 779–782. [CrossRef]
29. Kirchdoerfer, R.N.; Ward, A.B. Structure of the SARS-CoV nsp12 polymerase bound to nsp7 and nsp8 co-factors. *Nat. Commun.* **2019**, *10*, 2342. [CrossRef]
30. Mcdonald, S.M. RNA synthetic mechanisms employed by diverse families of RNA viruses. *Wiley Interdiscip. Rev. RNA* **2013**, *4*, 351–367. [CrossRef]
31. Van Hemert, M.J.; Van Den Worm, S.H.E.; Knoops, K.; Mommaas, A.M.; Gorbalenya, A.E.; Snijder, E.J. SARS-coronavirus replication/transcription complexes are membrane-protected and need a host factor for activity in vitro. *PLoS Pathog.* **2008**, *4*, e1000054. [CrossRef] [PubMed]
32. Lu, C.C.; Chen, M.Y.; Lee, W.S.; Chang, Y.L. Potential therapeutic agents against COVID-19: What we know so far. *J. Chin. Med. Assoc.* **2020**, *83*, 534–536. [CrossRef] [PubMed]
33. Sheahan, T.P.; Sims, A.C.; Zhou, S.; Graham, R.L.; Pruijssers, A.J.; Agostini, M.L.; Leist, S.R.; Schafer, A.; Dinnon, K.H.; Stevens, L.J.; et al. An orally bioavailable broad-spectrum antiviral inhibits SARS-CoV-2 in human airway epithelial cell cultures and multiple coronaviruses in mice. *Sci. Transl. Med.* **2020**, *12*, eabb5883. [CrossRef] [PubMed]
34. Hung, I.F.N.; Lung, K.C.; Tso, E.Y.K.; Liu, R.; Chung, T.W.H.; Chu, M.Y.; Ng, Y.Y.; Lo, J.; Chan, J.; Tam, A.R.; et al. Triple combination of interferon beta-1b, lopinavir–ritonavir, and ribavirin in the treatment of patients admitted to hospital with COVID-19: An open-label, randomised, phase 2 trial. *Lancet* **2020**, *395*, 1695–1704. [CrossRef]
35. Planas, D.; Veyer, D.; Baidaliuk, A.; Staropoli, I.; Guivel-Benhassine, F.; Rajah, M.M.; Planchais, C.; Porrot, F.; Robillard, N.; Puech, J.; et al. Reduced sensitivity of SARS-CoV-2 variant Delta to antibody neutralization. *Nature* **2021**, *596*, 276–280. [CrossRef]
36. Shelley, J.C.; Cholleti, A.; Frye, L.L.; Greenwood, J.R.; Timlin, M.R.; Uchimaya, M. Epik: A software program for pKa prediction and protonation state generation for drug-like molecules. *J. Comput. Aided. Mol. Des.* **2007**, *21*, 681–691. [CrossRef]
37. Harder, E.; Damm, W.; Maple, J.; Wu, C.; Reboul, M.; Xiang, J.Y.; Wang, L.; Lupyan, D.; Dahlgren, M.K.; Knight, J.L.; et al. OPLS3: A Force Field Providing Broad Coverage of Drug-like Small Molecules and Proteins. *J. Chem. Theory Comput.* **2016**, *12*, 281–296. [CrossRef]
38. Lan, J.; Ge, J.; Yu, J.; Shan, S.; Zhou, H.; Fan, S.; Zhang, Q.; Shi, X.; Wang, Q.; Zhang, L.; et al. Structure of the SARS-CoV-2 spike receptor-binding domain bound to the ACE2 receptor. *Nature* **2020**, *581*, 215–220. [CrossRef]
39. Adzhigirey, M.; Day, T.; Sherman, W.; Madhavi Sastry, G.; Annabhimoju, R. Protein and ligand preparation: Parameters, protocols, and influence on virtual screening enrichments. *J. Comput. Aided. Mol. Des.* **2013**, *27*, 221–234. [CrossRef]
40. Jacobson, M.P.; Pincus, D.L.; Rapp, C.S.; Day, T.J.F.; Honig, B.; Shaw, D.E.; Friesner, R.A. A Hierarchical Approach to All-Atom Protein Loop Prediction. *Proteins Struct. Funct. Bioinforma.* **2004**, *367*, 351–367. [CrossRef]
41. Friesner, R.A.; Banks, J.L.; Murphy, R.B.; Halgren, T.A.; Klicic, J.J.; Mainz, D.T.; Repasky, M.P.; Knoll, E.H.; Shelley, M.; Perry, J.K.; et al. Glide: A New Approach for Rapid, Accurate Docking and Scoring. 1. Method and Assessment of Docking Accuracy. *J. Med. Chem.* **2004**, *47*, 1739–1749. [CrossRef] [PubMed]
42. Halgren, T.A.; Murphy, R.B.; Friesner, R.A.; Beard, H.S.; Frye, L.L.; Pollard, W.T.; Banks, J.L. Glide: A New Approach for Rapid, Accurate Docking and Scoring. 2. Enrichment Factors in Database Screening. *J. Med. Chem.* **2004**, *47*, 1750–1759. [CrossRef] [PubMed]
43. Ahmad, J.; Ikram, S.; Ahmad, F.; Rehman, I.U.; Mushtaq, M. SARS-CoV-2 RNA Dependent RNA polymerase (RdRp)—A drug repurposing study. *Heliyon* **2020**, *6*, e04502. [CrossRef] [PubMed]
44. Du, J.; Sun, H.; Xi, L.; Li, J.; Yang, Y.; Liu, H.; Yao, X. Molecular modeling study of checkpoint kinase 1 inhibitors by multiple docking strategies and prime/MM-GBSA calculation. *J. Comput. Chem.* **2011**, *32*, 2800–2809. [CrossRef]
45. Lyne, P.D.; Lamb, M.L.; Saeh, J.C. Accurate prediction of the relative potencies of members of a series of kinase inhibitors using molecular docking and MM-GBSA scoring. *J. Med. Chem.* **2006**, *49*, 4805–4808. [CrossRef]
46. Li, J.; Abel, R.; Zhu, K.; Cao, Y.; Zhao, S.; Friesner, R.A. The VSGB 2.0 model: A next generation energy model for high resolution protein structure modeling. *Proteins Struct. Funct. Bioinforma.* **2011**, *79*, 2794–2812. [CrossRef]
47. Bowers, K.J.; Bowers, K.J.; Chow, E.; Xu, H.; Dror, R.O.; Eastwood, M.P.; Gregersen, B.A.; Klepeis, J.L.; Kolossvary, I.; Moraes, M.A.; et al. Scalable algorithms for molecular dynamics simulations on commodity clusters. In Proceedings of the SC '06: 2006 ACM/IEEE Conference on Supercomputing, Tampa, FL, USA, 11–17 November 2006.
48. Roos, K.; Wu, C.; Damm, W.; Reboul, M.; Stevenson, J.M.; Lu, C.; Dahlgren, M.K.; Mondal, S.; Chen, W.; Wang, L.; et al. OPLS3e: Extending Force Field Coverage for Drug-Like Small Molecules. *J. Chem. Theory Comput.* **2019**, *15*, 1863–1874. [CrossRef]
49. Jorgensen, W.L.; Chandrasekhar, J.; Madura, J.D.; Impey, R.W.; Klein, M.L. Comparison of simple potential functions for simulating liquid water. *J. Chem. Phys.* **1983**, *79*, 926–935. [CrossRef]

50. Schrödinger, L. *PyMol, The PyMOL Molecular Graphics System, Version 2.4*; Schrödinger, LLC: New York, NY, USA, 2020.
51. Thiruvengadam, R.; Awasthi, A.; Medigeshi, G.; Bhattacharya, S.; Mani, S.; Sivasubbu, S.; Shrivastava, T. Articles Effectiveness of ChAdOx1 nCoV-19 vaccine against SARS-CoV-2 infection during the delta (B.1.617.2) variant surge in India: A test-negative, case-control study and a mechanistic study of post-vaccination immune responses. *Lancet Infect. Dis.* **2021**, *3099*, 1–10. [CrossRef]
52. Public Health England. Technical Briefing 23. SARS-CoV-2 Variants of Concern and Variants under Investigation in England. 2021, pp. 1–61. Available online: https://assets.publishing.service.gov.uk/government/uploads/system/uploads/attachment_data/file/1018547/Technical_Briefing_23_21_09_16.pdf (accessed on 1 March 2022).
53. Abdool, S.S.; Abdool, Q. Omicron SARS-CoV-2 Variant: A New Chapter in the COVID-19 Pandemic. *Lancet* **2021**, *398*, 2126–2128. [CrossRef]
54. Cort, A.; Timur, M.; Ozdemir, E.; Kucuksayan, E.; Ozben, T. Synergistic anticancer activity of curcumin and bleomycin: An in vitro study using human malignant testicular germ cells. *Mol. Med. Rep.* **2012**, *5*, 1481–1486. [CrossRef] [PubMed]
55. Burgy, O.; Wettstein, G.; Bellaye, P.S.; Decologne, N.; Racoeur, C.; Goirand, F.; Beltramo, G.; Hernandez, J.F.; Kenani, A.; Camus, P.; et al. Deglycosylated bleomycin has the antitumor activity of bleomycin without pulmonary toxicity. *Sci. Transl. Med.* **2016**, *8*, 326ra20. [CrossRef] [PubMed]
56. Che, R.; Zhu, Q.; Yu, J.; Li, J.; Yu, J.; Lu, W. Syntheses of two kinds of disaccharide subunits of antitumor antibiotic bleomycins. *Tetrahedron* **2017**, *73*, 6172–6180. [CrossRef]
57. Cooper, I.; Atrakchi, D.; Walker, M.D.; Horovitz, A.; Fridkin, M.; Shechter, Y. Converting bleomycin into a prodrug that undergoes spontaneous reactivation under physiological conditions. *Toxicol. Appl. Pharmacol.* **2019**, *384*, 114782. [CrossRef]
58. Zhang, Z.F.; Fan, S.H.; Zheng, Y.L.; Lu, J.; Wu, D.M.; Shan, Q.; Hu, B. Troxerutin improves hepatic lipid homeostasis by restoring NAD^+-depletion-mediated dysfunction of lipin 1 signaling in high-fat diet-treated mice. *Biochem. Pharmacol.* **2014**, *91*, 74–86. [CrossRef]
59. Saif, M.W.; Parikh, R.; Ray, D.; Kaye, J.A.; Kurosky, S.K.; Thomas, K.; Ramirez, R.A.; Halfdanarson, T.R.; Beveridge, T.J.R.; Mirakhur, B.; et al. Medical record review of transition to lanreotide following octreotide for neuroendocrine tumors. *J. Gastrointest. Oncol.* **2019**, *10*, 674–687. [CrossRef]
60. Caron, P.J.; Bevan, J.S.; Petersenn, S.; Houchard, A.; Sert, C.; Webb, S.M. Effects of lanreotide Autogel primary therapy on symptoms and quality-of-life in acromegaly: Data from the PRIMARYS study. *Pituitary* **2016**, *19*, 149–157. [CrossRef]
61. Biermasz, N.R. New medical therapies on the horizon: Oral octreotide. *Pituitary* **2017**, *20*, 149–153. [CrossRef]
62. Zafer, M.M.; El-Mahallawy, H.A.; Abdulhak, A.; Amin, M.A.; Al-Agamy, M.H.; Radwan, H.H. Emergence of colistin resistance in multidrug-resistant Klebsiella pneumoniae and Escherichia coli strains isolated from cancer patients. *Ann. Clin. Microbiol. Antimicrob.* **2019**, *18*, 40. [CrossRef]
63. Nation, R.L.; Li, J. Colistin in the 21st century. *Curr. Opin. Infect. Dis.* **2009**, *22*, 535–543. [CrossRef]
64. Stokowa-Sołtys, K.; Barbosa, N.A.; Kasprowicz, A.; Wieczorek, R.; Gaggelli, N.; Gaggelli, E.; Valensin, G.; Wrzesiński, J.; Ciesiołka, J.; Kuliński, T.; et al. Studies of viomycin, an anti-tuberculosis antibiotic: Copper(II) coordination, DNA degradation and the impact on delta ribozyme cleavage activity. *Dalt. Trans.* **2016**, *45*, 8645–8658. [CrossRef] [PubMed]
65. Grossman, R.I.; Modic, M.T. A randomized comparison of iodixanol and iohexol in adult intracranial computed tomography scanning. *Acad. Radiol.* **1996**, *3* (Suppl S3), S488–S494. [CrossRef]
66. Seong, J.M.; Choi, N.K.; Lee, J.; Chang, Y.; Kim, Y.J.; Yang, B.R.; Jin, X.M.; Kim, J.Y.; Park, B.J. Comparison of the safety of seven iodinated contrast media. *J. Korean Med. Sci.* **2013**, *28*, 1703–1710. [CrossRef] [PubMed]
67. Manoharan, Y.; Haridas, V.; Vasanthakumar, K.C. Curcumin: A Wonder Drug as a Preventive Measure for COVID19 Management. *Indian J. Clin. Biochem.* **2020**, *35*, 373–375. [CrossRef]
68. Gupta, S.C.; Patchva, S.; Aggarwal, B.B. Therapeutic roles of curcumin: Lessons learned from clinical trials. *AAPS J.* **2013**, *15*, 195–218. [CrossRef]
69. Kaufman, A.J.; Concepcion, R.; Kirchner, F.K.; McDougal, W.S.; Winfield, A.C. Ioversol for intravenous urography: A comparison study. *Urol. Radiol. A J. Diagn. Imaging* **1990**, *12*, 56–60. [CrossRef]
70. Boyer, T.D. Advances in Hepatology. *Gastroenterol. Hepatol.* **2007**, *3*, 773–774.
71. Bello, M.; Martínez-Muñoz, A.; Balbuena-Rebolledo, I. Identification of saquinavir as a potent inhibitor of dimeric SARS-CoV2 main protease through MM/GBSA. *J. Mol. Model.* **2020**, *26*, 340. [CrossRef]
72. Noble, S.; Faulds, D. Saquinavir. *Drug Eval.* **1996**, *52*, 93–112. [CrossRef]
73. Weidner, L.D.; Fung, K.L.; Kannan, P.; Moen, J.K.; Kumar, J.S.; Mulder, J.; Innis, R.B.; Gottesman, M.M.; Hall, M.D. Tariquidar is an inhibitor and not a substrate of human and mouse P-glycoprotein. *Drug Metab. Dispos.* **2016**, *44*, 275–282. [CrossRef]
74. Chung, B.H.; Horie, S.; Chiong, E. Clinical studies investigating the use of leuprorelin for prostate cancer in Asia. *Prostate Int.* **2020**, *8*, 1–9. [CrossRef] [PubMed]
75. Kundu, S.T.; Grzeskowiak, C.L.; Fradette, J.J.; Gibson, L.A.; Rodriguez, L.B.; Creighton, C.J.; Scott, K.L.; Gibbons, D.L. TMEM106B drives lung cancer metastasis by inducing TFEB-dependent lysosome synthesis and secretion of cathepsins. *Nat. Commun.* **2018**, *9*, 2731. [CrossRef] [PubMed]
76. Siklos, M.; BenAissa, M.; Thatcher, G.R.J. Cysteine proteases as therapeutic targets: Does selectivity matter? A systematic review of calpain and cathepsin inhibitors. *Acta Pharm. Sin. B* **2015**, *5*, 506–519. [CrossRef]

77. Heiser, K.; McLean, P.F.; Davis, C.; Fogelson, B.; Gordon, H.B.; Jacobson, P.; Hurst, B.; Miller, B.; Alfa, R.W.; Earnshaw, B.A.; et al. Identification of potential treatments for COVID-19 through artificial intelligence-enabled phenomic analysis of human cells infected with SARS-CoV-2. *bioRxiv* **2020**. [CrossRef]
78. Mahanta, S.; Chowdhury, P.; Gogoi, N.; Goswami, N.; Borah, D.; Kumar, R.; Chetia, D.; Borah, P.; Alak, K.; Gogoi, B. Potential anti-viral activity of approved repurposed drug against main protease of SARS- CoV-2: An in silico based approach. *J. Biomol. Struct. Dyn.* **2021**, *39*, 3802–3811. [CrossRef]
79. Chakraborti, S.; Bheemireddy, S.; Srinivasan, N. Repurposing drugs against the main protease of SARS-CoV-2: Mechanism-based insights supported by available laboratory and clinical data. *Mol. Omi.* **2020**, *16*, 474–491. [CrossRef] [PubMed]
80. George, P.M.; Wells, A.U.; Jenkins, R.G. Personal View Pulmonary fibrosis and COVID-19: The potential role for antifibrotic therapy. *Lancet Respir.* **2020**, *8*, 807–815. [CrossRef]
81. Maffucci, I.; Contini, A. In Silico Drug Repurposing for SARS-CoV-2 Main Proteinase and Spike Proteins. *J. Proteome Res.* **2020**, *19*, 4637–4648. [CrossRef]
82. Hajialyani, M.; Farzaei, M.H.; Echeverría, J.; Nabavi, S.M.; Uriarte, E.; Eduardo, S.S. Hesperidin as a neuroprotective agent: A review of animal and clinical evidence. *Molecules* **2019**, *24*, 648. [CrossRef]
83. Lalani, S.; Ti, L.; Laa, C. Antiviral peptides against Enterovirus A71 causing hand, foot and mouth disease. *Peptides* **2021**, *136*, 170443. [CrossRef]
84. O'Brien, J.J.; Campoli-Richards, D.M. Acyclovir: An Updated Review of its Antiviral Activity, Pharmacokinetic Properties and Therapeutic Efficacy. *Drugs* **1989**, *37*, 233–309. [CrossRef] [PubMed]
85. Miller, J.L. Iron deficiency anemia: A common and curable disease. *Cold Spring Harb. Perspect. Med.* **2013**, *3*, a011866. [CrossRef] [PubMed]
86. Sanchez, R.I.; Fillgrove, K.L.; Yee, K.L.; Liang, Y.; Lu, B.; Tatavarti, A.; Liu, R.; Anderson, M.S.; Behm, M.O.; Fan, L.; et al. Characterisation of the absorption, distribution, metabolism, excretion and mass balance of doravirine, a non-nucleoside reverse transcriptase inhibitor in humans. *Xenobiotica* **2019**, *49*, 422–432. [CrossRef]
87. Van Gorkom, B.A.P.; Karrenbeld, A.; Van der Sluis, T.; Zwart, N.; De Vries, E.G.E.; Kleibeuker, J.H. Apoptosis induction by sennoside laxatives in man: Escape from a protective mechanism during chronic sennoside use? *J. Pathol.* **2001**, *194*, 493–499. [CrossRef] [PubMed]
88. Esposito, F.; Carli, I.; Del Vecchio, C.; Xu, L.; Corona, A.; Grandi, N.; Piano, D.; Maccioni, E.; Distinto, S.; Parolin, C.; et al. Sennoside A, derived from the traditional chinese medicine plant Rheum L., is a new dual HIV-1 inhibitor effective on HIV-1 replication. *Phytomedicine* **2016**, *23*, 1383–1391. [CrossRef] [PubMed]
89. Zempleni, J.; Galloway, J.R.; McCormick, D.B. Pharmacokinetics of orally and intravenously administered riboflavin in healthy humans. *Am. J. Clin. Nutr.* **1996**, *63*, 54–66. [CrossRef]
90. Islam, R.; Parves, M.R.; Paul, A.S.; Uddin, N.; Rahman, M.S.; Mamun, A.A.; Hossain, M.N.; Ali, M.A.; Halim, M.A. A molecular modeling approach to identify effective antiviral phytochemicals against the main protease of SARS-CoV-2. *J. Biomol. Struct. Dyn.* **2021**, *39*, 3213–3224. [CrossRef]
91. Chen, Y.W.; Yiu, C.P.B.; Wong, K.Y. Prediction of the SARS-CoV-2 (2019-nCoV) 3C-like protease (3CLpro) structure: Virtual screening reveals velpatasvir, ledipasvir, and other drug repurposing candidates. *F1000Research* **2020**, *9*, 129. [CrossRef] [PubMed]
92. Mengist, H.M.; Dilnessa, T.; Jin, T. Structural Basis of Potential Inhibitors Targeting SARS-CoV-2 Main Protease. *Front. Chem.* **2021**, *9*, 622898. [CrossRef]
93. Jain, R.; Mujwar, S. Repurposing metocurine as main protease inhibitor to develop novel antiviral therapy for COVID-19. *Struct. Chem.* **2020**, *31*, 2487–2499. [CrossRef]
94. Xue, X.; Yang, H.; Shen, W.; Zhao, Q.; Li, J.; Yang, K.; Chen, C.; Jin, Y.; Bartlam, M.; Rao, Z. Production of Authentic SARS-CoV Mpro with Enhanced Activity: Application as a Novel Tag-cleavage Endopeptidase for Protein Overproduction. *J. Mol. Biol.* **2007**, *366*, 965–975. [CrossRef] [PubMed]
95. Cheng, F.-J.; Huynh, T.-K.; Yang, C.-S.; Shen, Y.-C.; Tu, C.-Y.; Wu, Y.-C.; Tang, C.-H.; Huang, W.-C.; Chen, Y.; Ho, C.-Y. Hesperidin is a potential inhibitor against SARS-CoV-2 infection. *Nutrients* **2021**, *13*, 2800. [CrossRef] [PubMed]
96. Santos, I.D.; Grosche, V.R.; Bergamini, F.R.G.; Sabino-Silva, R.; Jardim, A.C.G. Antivirals against Coronaviruses: Candidate Drugs for SARS-CoV-2 Treatment? *Front. Microbiol.* **2020**, *11*, 1818. [CrossRef] [PubMed]
97. Peters, H.L.; Jochmans, D.; De Wilde, A.H.; Posthuma, C.C.; Snijder, E.J.; Neyts, J.; Seley-Radtke, K.L. Design, synthesis and evaluation of a series of acyclic fleximer nucleoside analogues with anti-coronavirus activity. *Bioorg. Med. Chem. Lett.* **2015**, *25*, 2923–2926. [CrossRef]
98. Unal, M.A.; Bitirim, C.V.; Summak, G.Y.; Bereketoglu, S.; Zeytin, I.C.; Besbinar, O.; Gurcan, C.; Aydos, D.; Goksoy, E.; Kocakaya, E.; et al. Ribavirin shows antiviral activity against sars-cov-2 and downregulates the activity of tmprss2 and the expression of ace2 in vitro. *Can. J. Physiol. Pharmacol.* **2021**, *99*, 449–460. [CrossRef]
99. DeJong, C.; Spinelli, M.A.; Okochi, H.; Gandhi, M. Tenofovir-based PrEP for COVID-19: An untapped opportunity? *Aids* **2021**, *35*, 1509–1511. [CrossRef]
100. Harvey, W.T.; Carabelli, A.M.; Jackson, B.; Gupta, R.K.; Thomson, E.C.; Harrison, E.M.; Ludden, C.; Reeve, R.; Rambaut, A.; Peacock, S.J.; et al. SARS-CoV-2 variants, spike mutations and immune escape. *Nat. Rev. Microbiol.* **2021**, *19*, 409–424. [CrossRef]

101. Deng, X.; Garcia-Knight, M.A.; Khalid, M.M.; Servellita, V.; Wang, C.; Morris, M.; Sotomayor-González, A.; Glasner, D.R.; Reyes, K.; Gliwa, A.; et al. Transmission, infectivity, and antibody neutralization of an emerging SARS-CoV-2 variant in California carrying a L452R spike protein mutation. *MedRxiv* **2021**. [CrossRef]
102. Joshi, M.; Kumar, M.; Srivastava, V.; Kumar, D.; Pandit, R.; Joshi, C.G. First detection of SARS-CoV-2 Delta variant (B.1.617.2) in the wastewater of (Ahmedabad), India. *MedRxiv* **2021**. [CrossRef]
103. Yi, C.; Sun, X.; Ye, J.; Ding, L.; Liu, M.; Yang, Z.; Lu, X.; Zhang, Y.; Ma, L.; Gu, W.; et al. Key residues of the receptor binding motif in the spike protein of SARS-CoV-2 that interact with ACE2 and neutralizing antibodies. *Cell. Mol. Immunol.* **2020**, *17*, 621–630. [CrossRef]
104. Ugur, I.; Marion, A. Molecular modelling reveals eight novel druggable binding sites in SARS-CoV-2's spike protein. *ChemRxiv* **2020**. [CrossRef]
105. Moore, J.P.; Offit, P.A. SARS-CoV-2 Vaccines and the Growing Threat of Viral Variants. *JAMA-J. Am. Med. Assoc.* **2021**, *325*, 821–822. [CrossRef] [PubMed]
106. Wang, Z.; Schmidt, F.; Weisblum, Y.; Muecksch, F.; Barnes, C.O.; Finkin, S.; Schaefer-Babajew, D.; Cipolla, M.; Gaebler, C.; Lieberman, J.A.; et al. mRNA vaccine-elicited antibodies to SARS-CoV-2 and circulating variants. *Nature* **2021**, *592*, 616–622. [CrossRef] [PubMed]
107. Mannar, D.; Saville, J.W.; Zhu, X.; Srivastava, S.S.; Berezuk, A.M.; Zhou, S.; Tuttle, K.S.; Kim, A.; Li, W.; Dimitrov, D.S.; et al. Structural analysis of receptor binding domain mutations in SARS-CoV-2 variants of concern that modulate ACE2 and antibody binding. *Cell Rep.* **2021**, *37*, 110156. [CrossRef]
108. Hillen, H.S.; Kokic, G.; Farnung, L.; Dienemann, C.; Tegunov, D.; Cramer, P. Structure of replicating SARS-CoV-2 polymerase. *Nature* **2020**, *584*, 154–156. [CrossRef]
109. Miell, J.; Dhanjal, P.; Jamookeeah, C. Evidence for the use of demeclocycline in the treatment of hyponatraemia secondary to SIADH: A systematic review. *Int. J. Clin. Pract.* **2015**, *69*, 1396–1417. [CrossRef]
110. Hasan, M.K.; Kamruzzaman, M.; Bin Manjur, O.H.; Mahmud, A.; Hussain, N.; Alam Mondal, M.S.; Hosen, M.I.; Bello, M.; Rahman, A. Structural analogues of existing anti-viral drugs inhibit SARS-CoV-2 RNA dependent RNA polymerase: A computational hierarchical investigation. *Heliyon* **2021**, *7*, e06435. [CrossRef]
111. Gordon, C.J.; Tchesnokov, E.P.; Schinazi, R.F.; Götte, M. Molnupiravir promotes SARS-CoV-2 mutagenesis via the RNA template. *J. Biol. Chem.* **2021**, *297*, 100770. [CrossRef]
112. Kabinger, F.; Stiller, C.; Schmitzová, J.; Dienemann, C.; Kokic, G.; Hillen, H.S.; Höbartner, C.; Cramer, P. Mechanism of molnupiravir-induced SARS-CoV-2 mutagenesis. *Nat. Struct. Mol. Biol.* **2021**, *28*, 740–746. [CrossRef]
113. Elfiky, A.A. Ribavirin, Remdesivir, Sofosbuvir, Galidesivir, and Tenofovir against SARS-CoV-2 RNA dependent RNA polymerase (RdRp): A molecular docking study. *Life Sci.* **2020**, *253*, 117592. [CrossRef]
114. Kim, S.H.; MacIntyre, D.A.; Hanyaloglu, A.C.; Blanks, A.M.; Thornton, S.; Bennett, P.R.; Terzidou, V. The Oxytocin Receptor Antagonist, Atosiban, Activates pro-Inflammatory Pathways in Human Amnion via G(αi) Signalling. *Mol. Cell. Endocrinol.* **2016**, *420*, 11–23. [CrossRef] [PubMed]
115. Pandey, P.; Khan, F. A Mechanistic Review of the Anticancer Potential of Hesperidin, a Natural Flavonoid from Citrus Fruits. *Nutr. Res.* **2021**, *92*, 21–31. [CrossRef] [PubMed]
116. Radu, D.; Åhlin, A.; Svanborg, P.; Lindefors, N. Anxiogenic Effects of the CCK B Agonist Pentagastrin in Humans and Dose-Dependent Increase in Plasma C-Peptide Levels. *Psychopharmacology* **2002**, *161*, 396–403. [CrossRef] [PubMed]
117. Aggerbeck, M.; Guellaën, G.; Hanoune, J. N-Aralkyl Substitution Increases the Affinity of Adrenergic Drugs for the Alpha-Adrenoceptor in Rat Liver. *Br. J. Pharmacol.* **1979**, *65*, 155–159. [CrossRef] [PubMed]
118. Ackerson, N.O.B.; Liberatore, H.K.; Plewa, M.J.; Richardson, S.D.; Ternes, T.A.; Duirk, S.E. Disinfection Byproducts and Halogen-Specific Total Organic Halogen Speciation in Chlorinated Source Waters – The Impact of Iopamidol and Bromide. *J. Environ. Sci.* **2020**, *89*, 90–101. [CrossRef]
119. Meijenhorst, G.C.; de Bruin, J.N. Hexabrix (ioxaglate), a New Low Osmolality Contrast Agent for Lumbar Epidural Double-Catheter Venography. *Neuroradiology* **1980**, *20*, 29–32. [CrossRef]
120. Garriga, C.; Pérez-Elías, M.J.; Delgado, R.; Ruiz, L.; Nájera, R.; Pumarola, T.; del Mar Alonso-Socas, M.; García-Bujalance, S.; Menéndez-Arias, L. Mutational Patterns and Correlated Amino Acid Substitutions in the HIV-1 Protease after Virological Failure to Nelfinavir- and Lopinavir/ritonavir-Based Treatments. *J. Med. Virol.* **2007**, *79*, 1617–1628. [CrossRef]
121. Karlgren, M.; Vildhede, A.; Norinder, U.; Wisniewski, J.R.; Kimoto, E.; Lai, Y.; Haglund, U.; Artursson, P. Classification of Inhibitors of Hepatic Organic Anion Transporting Polypeptides (OATPs): Influence of Protein Expression on Drug–Drug Interactions. *J. Med. Chem.* **2012**, *55*, 4740–4763. [CrossRef]
122. Zwiener, C.; Glauner, T.; Sturm, J.; Wörner, M.; Frimmel, F.H. Electrochemical Reduction of the Iodinated Contrast Medium Iomeprol: Iodine Mass Balance and Identification of Transformation Products. *Anal. Bioanal. Chem.* **2009**, *395*, 1885–1892. [CrossRef]
123. Chow, S.L.; Ng, T.M.H.; Litwinski, R.A.; Kangavari, S.; Weiss, M. Effect of Iodixanol and Ioxilan on QT Interval and Renal Function in Patients with Systolic Heart Failure. *Int. J. Cardiol.* **2012**, *154*, 17–21. [CrossRef]
124. Diaz-Montero, C.M.; Wang, Y.; Shao, L.; Feng, W.; Zidan, A.-A.; Pazoles, C.J.; Montero, A.J.; Zhou, D. The Glutathione Disulfide Mimetic NOV-002 Inhibits Cyclophosphamide-Induced Hematopoietic and Immune Suppression by Reducing Oxidative Stress. *Free Radic. Biol. Med.* **2012**, *52*, 1560–1568. [CrossRef] [PubMed]

125. Stover, P.J.; Field, M.S. Trafficking of Intracellular Folates. *Adv. Nutr.* **2011**, *2*, 325–331. [CrossRef] [PubMed]
126. Chuang, V.T.G.; Suno, M. Levoleucovorin as Replacement for Leucovorin in Cancer Treatment. *Ann. Pharmacother.* **2012**, *46*, 1349–1357. [CrossRef] [PubMed]
127. Adolph, J.M.G.; Engelkamp, H.; Herbig, W.; Peters, P.E.; Wenzel-Hora, B.I. Iotrolan in Urography: Efficacy and Tolerance in Comparison with Iohexol and Iopamidol. *Eur. Radiol.* **1995**, *5*, S63–S68. [CrossRef]
128. Gan, X.-D.; Wei, B.-Z.; Fang, D.; Fang, Q.; Li, K.-Y.; Ding, S.-L.-Y.; Peng, S.; Wan, J. Efficacy and Safety Analysis of New P2Y12 Inhibitors versus Clopidogrel in Patients with Percutaneous Coronary Intervention: A Meta-Analysis. *Curr. Med. Res. Opin.* **2015**, *31*, 2313–2323. [CrossRef]
129. Holleran, J.L.; Parise, R.A.; Guo, J.; Kiesel, B.F.; Taylor, S.E.; Percy Ivy, S.; Chu, E.; Beumer, J.H. Quantitation of Iohexol, a Glomerular Filtration Marker, in Human Plasma by LC–MS/MS. *J. Pharm. Biomed. Anal.* **2020**, *189*, 113464. [CrossRef]
130. Dhondt, L.; Croubels, S.; De Cock, P.; Dhont, E.; De Baere, S.; De Paepe, P.; Devreese, M. Volumetric Absorptive Microsampling as Alternative Sampling Technique for Renal Function Assessment in the Paediatric Population Using Iohexol. *J. Chromatogr. B Anal. Technol. Biomed. Life Sci.* **2021**, *1171*, 122623. [CrossRef]
131. Hofmann, M.; Maecke, H.; Börner, A.; Weckesser, E.; Schöffski, P.; Oei, M.; Schumacher, J.; Henze, M.; Heppeler, A.; Meyer, G.; et al. Biokinetics and Imaging with the Somatostatin Receptor PET Radioligand 68Ga-DOTATOC: Preliminary Data. *Eur. J. Nucl. Med.* **2001**, *28*, 1751–1757. [CrossRef]
132. Carlquist, M.; Frejd, T.; Gorwa-Grauslund, M.F. Flavonoids as Inhibitors of Human Carbonyl Reductase 1. *Chem. Biol. Interact.* **2008**, *174*, 98–108. [CrossRef]
133. Zoghbi, G.J.; Iskandrian, A.E. Selective Adenosine Agonists and Myocardial Perfusion Imaging. *J. Nucl. Cardiol.* **2012**, *19*, 126–141. [CrossRef]
134. Hirshfeld, J.W., Jr.; Wieland, J.; Davis, C.A.; Giles, B.D.; Passione, D.; Ray, M.B.; Ripley, N.S. Hemodynamic and Electrocardiographic Effects of Ioversol during Cardiac Angiography. *Investig. Radiol.* **1989**, *24*, 138–144. [CrossRef] [PubMed]
135. Peters, F.; Ellermann, I.; Steinbicker, A.U. Intravenous Iron for Treatment of Anemia in the 3 Perisurgical Phases: A Review and Analysis of the Current Literature. *Anesth. Analg.* **2018**, *126*, 1268–1282. [CrossRef] [PubMed]
136. Geisser, P.; Burckhardt, S. The Pharmacokinetics and Pharmacodynamics of Iron Preparations. *Pharmaceutics* **2011**, *3*, 12–33. [CrossRef]
137. Charytan, C.; Levin, N.; Al-Saloum, M.; Hafeez, T.; Gagnon, S.; Van Wyck, D.B. Efficacy and Safety of Iron Sucrose for Iron Deficiency in Patients with Dialysis-Associated Anemia: North American Clinical Trial. *Am. J. Kidney Dis.* **2001**, *37*, 300–307. [CrossRef] [PubMed]
138. Leonard, R.; Yellowlees, A.; Mansi, J.; Fallowfield, L.; Jenkins, V. The Affect of Goserelin on the QoL of Women Having Chemotherapy for EBC: Results from the OPTION Trial. *Breast* **2020**, *52*, 122–131.
139. Aljabri, B.; Lilleby, W.; Switlyk, M.D.; Tafjord, G. Restart of Androgen Deprivation Therapy after Goserelin Induced Pituitary Apoplexy in a Patient with Disseminated Prostate Cancer a Case Report and Five-Years Follow-Up. *Urol. Case Rep.* **2021**, *37*, 101648. [CrossRef]
140. Tuyen, D.T.; Yew, G.Y.; Cuong, N.T.; Hoang, L.T.; Yen, H.T.; Thao, P.T.H.; Thao, N.T.; le Thanh, N.S.; Trang, N.T.H.; Trung, N.T.; et al. Selection, Purification, and Evaluation of Acarbose−an α-Glucosidase Inhibitor from Actinoplanes Sp. *Chemosphere* **2021**, *265*, 129167. [CrossRef]
141. Wang, Z.; Wang, J.; Hu, J.; Chen, Y.; Dong, B.; Wang, Y. A Comparative Study of Acarbose, Vildagliptin and Saxagliptin Intended for Better Efficacy and Safety on Type 2 Diabetes Mellitus Treatment. *Life Sci.* **2021**, *274*, 119069. [CrossRef]
142. Loho, T.; Dharmayanti, A. Colistin: An Antibiotic and Its Role in Multiresistant Gram-Negative Infections. *Acta Med. Indones.* **2015**, *47*, 157–168. [PubMed]
143. Weiner, C.P.; Buhimschi, C. *Drugs for Pregnant and Lactating Women E-Book*; Elsevier Health Sciences: Hoboken, NJ, USA, 2009; ISBN 9781437721362.
144. Barza, M. Imipenem: First of a New Class of Beta-Lactam Antibiotics. *Ann. Intern. Med.* **1985**, *103*, 552–560. [CrossRef] [PubMed]
145. Deeks, E.D.; Perry, C.M. Zoledronic Acid. *Drugs Aging* **2008**, *25*, 963–986. [CrossRef] [PubMed]
146. Wellington, K.; Goa, K.L. Zoledronic Acid. *Drugs* **2012**, *63*, 417–437. [CrossRef]
147. Zhong, X.; Ma, Z.; Su, Y.; Li, Z.; Liao, Y.; Pan, X.; Zang, L.; Zhou, S. Flavin Adenine Dinucleotide Ameliorates Hypertensive Vascular Remodeling via Activating Short Chain Acyl-CoA Dehydrogenase. *Life Sci.* **2020**, *258*, 118156. [CrossRef]
148. Bhowmick, N.A.; Oft, J.; Dorff, T.; Pal, S.; Agarwal, N.; Figlin, R.A.; Posadas, E.M.; Freedland, S.J.; Gong, J. COVID-19 and Androgen-Targeted Therapy for Prostate Cancer Patients. *Endocr. Relat. Cancer* **2020**, *27*, R281–R292. [CrossRef]
149. Müller, J.; Jewell, K.S.; Schulz, M.; Hermes, N.; Ternes, T.A.; Drewes, J.E.; Hübner, U. Capturing the Oxic Transformation of Iopromide – A Useful Tool for an Improved Characterization of Predominant Redox Conditions and the Removal of Trace Organic Compounds in Biofiltration Systems? *Water Res.* **2019**, *152*, 274–284. [CrossRef]